Detector performance studies and particle identification with PHOS

11th December 2005

G. Conesa[1], H. Delagrange[2], J. Díaz[1], Y. Kharlov[3], D. Peressounko[4], Y. Schutz[2,5]

Abstract

The ALICE experiment at LHC will detect and identify photons, electrons and light neutral-mesons with the PHOS detector. We present the PHOS performance and particle identification methods in different particle environments and detector configurations.

Contents

[1] IFIC (Centro Mixto Universidad de Valencia-CSIC), Valencia, Spain
[2] SUBATECH, UMR6457 (Ecole des Mines-IN2P3/CNRS-Université de Nantes), BP20722, 44307 Nantes CEDEX 3, France
[3] Institute for High Energy Physics, Protvino, Russia
[4] RRC Kurchatov Institute, Moscow, Russia
[5] CERN, Genève, Switzerland

Introduction

The role of PHOS in the ALICE experiment is to detect and identify real photons and measure with high resolution their 4-momentum with the prospect to perform the physics programs exploiting direct photons and light neutral mesons (π^0 and η mesons mainly) as privileged probes. The unique ability of PHOS to measure and identify particles over a broad dynamic range in transverse momentum will enable to access key information on the soft and hard processes occurring in pp, pA and AA collisions at LHC energies. Although the detection of photons is straightforward, their unambiguous identification, among the abundantly produced particles, constitutes a first challenge. A second one is the discrimination between direct and decay photons, which are mixed in a ratio of about one to ten. To respond to these challenges PHOS has been designed to match the following requirements:

- A high discrimination power between photons and any other kind of particle, charged and neutral baryons, charged hadrons and electrons;

- A high energy and position resolution and consequently a high mass resolution in the two-photon invariant mass spectrum;

- A geometrical acceptance sufficient to measure neutral mesons down to low transverse momenta and to collect statistically-significant data for the rare high-momentum particles.

We shall first describe the characteristics of PHOS which allow to meet these criteria. We shall then discuss the various steps to simulate the PHOS response: hits from the tracking algorithm are converted into digits which in turn are processed by the reconstruction algorithm to produce reconstructed particles. The simulated intrinsic properties of PHOS, matched to data from in-beam measurements, are presented. We examine how the various parameters are modified in the realistic environment of the ALICE experiment. Finally we discuss identification methods for neutral mesons and direct photons.

1   Detector description

The photon spectrometer PHOS is optimized for the measurement, with high energy and spatial resolution, of photons and of light neutral mesons (π^0 and η) through their two-photon decay. Particles will be efficiently identified over a wide dynamic range, spanning the domain from a few hundreds of MeV/c up to several tens of GeV/c. PHOS, acting as a calorimeter, gives also an access to global observables of interest for event characterization, such as the electromagnetic transverse energy and multiplicity at mid-rapidity. PHOS is described in details in [1, 2]. It consists (Fig. 1) of an electromagnetic calorimeter (EMC) [1], and a charged-particle detector acting as a veto (CPV) [1], [3].

- EMC is divided into five modules equipped each with 64 (across the beam direction) by 56 (along the beam direction) Lead-Tungstate PbWO$_4$ scintillator crystals. Each crystal is an 18 cm long parallelepiped, equivalent to 20 units of radiation length (X_0 [PbWO$_4$] = 0.89 cm). Its squared cross-section of 22×22 mm^2, corresponds to 90% of the Molière radius, (r_M[PbWO$_4$] = 20 mm). PHOS is located inside the ALICE solenoid magnet at a distance of 4.6 m and at azimuth angles ±40.7°,±20.3°, and 0°. Each module covers about one quarter of a unit in pseudo-rapidity, $|\eta| \leq 0.13$ and 17.8° in azimuth angle. The scintillation light, in the visible near UV-wavelength range, is detected by a 5×5 mm^2 avalanche photo-diode (APD) whose signal is processed by a low-noise pre-amplifier. The calorimeter is operated at $-25°$ C, stabilized to ±0.3°C, to optimize the scintillation light output and to minimize the
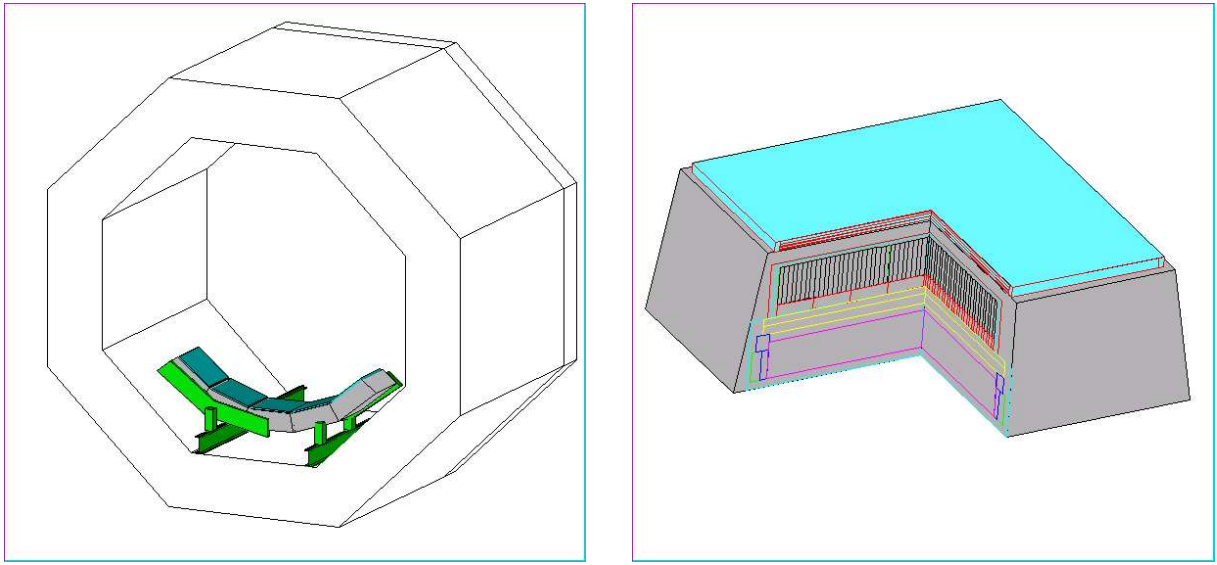
3

Figure 1: View of PHOS as described in AliRoot v3.06: PHOS inside the ALICE solenoid magnet (left), one PHOS block (right).

noise level from the APD. The electronic chain associated to each crystal delivers two energy signals with different amplification factors, and one timing signal.

- CPV consists of multi-wire proportional chambers with cathode pad read-out. Each calorimeter module is covered by a CPV module with an active area of 144.6×126.6 cm^2. It is 1.4 cm deep and filled with a gas mixture 80% Ar and 20% CO_2. The total thickness is 5.4 cm. Low-mass construction materials are used to minimize the material budget. The anode wires of the proportional chamber are strung 7 mm above the cathode along the beam direction with a pitch of 5.65 mm. The cathode is segmented in 56 (along beam direction)$\times$128 (across beam direction) rectangular pads of 2.26×1.13 cm^2. The charge induced on the cathode pads by avalanche near the relevant anode wire due to passage of a charged particle through the detector is read out by GASSIPLEX chips integrated on the detector front plane.

2 Simulation parameters

The exact geometry of PHOS is implemented in the AliRoot simulation package. The energy deposition in the active materials is calculated by the tracking algorithm (GEANT3) and is converted into digitized information comparable to real raw-data.

- The algorithm records at each step of the tracking a hit described by the deposited energy, the position, the time and the primary particle which has generated the hit. The deposited energy, E_d, is converted into a signal amplitude. The mean number

4

of scintillation photons, $\langle N_\gamma \rangle$, collected by the APD is calculated as:

$$\langle N_\gamma \rangle = E_d \widetilde{N_\gamma} \varepsilon_{\mathrm{APD}} e^{-Ad}$$

where $\widetilde{N_\gamma} = 4.7 \times 10^4\, \gamma$ GeV is the average number of scintillation photons per unit of deposited energy, $\varepsilon_{\mathrm{APD}} = 0.0266$ is the APD photo-efficiency, $A{=}0.0045$ is the attenuation factor of scintillation photons and d is the distance of the hit to the APD. The amplitude, $\mathcal{A}$, of the APD signal is calculated from n_γ, randomly selected according to a Poisson distribution with mean value $\langle N_\gamma \rangle$:

$$\mathcal{A} = n_\gamma G_{\mathrm{APD}} C$$

where $G_{\mathrm{APD}} = 300$ is the APD photo-electron gain factor and $C = 0.13418/\widetilde{N_\gamma}$ a calibration factor that converts photo-electrons into GeV. Since particles entering the calorimeter develop an electromagnetic shower and thus a huge number of tracks and hits, the PHOS algorithm only stores one hit per primary particle and per active volume. A PHOS hit thus corresponds to the summed energy deposited by a given primary particle in a single crystal and the time corresponds to the time at which the particle entered the volume: a primary particle can generate several hits in different volumes and there can be several hits in a single volume originating from different primary particles.

The energy, E_d, deposited by an ionizing particle in the active gas volume of CPV, is proportional to the ionization charge Q collected around the nearest anode wire: $Q = AE_d$. The collected charge is expressed in arbitrary units, and for simplicity A is taken equal to 1. When the track is inclined several anode wires can collect a charge which is proportional to the projection of the inclined track onto the CPV cathode plane. The charge distribution on the cathode plane is calculated according to the electrostatic formula:

$$\sigma(x') = \frac{Q}{\pi} \sum_{i=0}^{\infty} (-1)^i \frac{2i+1}{x'^2 + (2i+1)^2}$$

where $x' = x/d$, x is a distance from the charge on the cathode plane, d is the anode-to-cathode distance and i is the pad number. This charge distribution function allows to calculate the charge induced in each pad. The CPV hits are calculated from this distribution.

- Summable digits are constructed as a copy of hits. For hits with a deposited energy below a given threshold ($E_{\mathrm{th}}^{\mathrm{prim}} = 1$ MeV) the reference to the preliminary is omitted to reduce the number of primary particles attached to the same digit.

- To construct digits, first a random Gaussian noise (with a mean value of 4 MeV equivalent deposited energy for EMC and 0.01 units for CPV) is added to all active elements, whether they have been hit or not. Summable digits in the same active volume are merged into a single digit by summing the deposited energy. The time is calculated in a way that mimics the function of a leading-edge discriminator with a rise of $t_{\mathrm{rise}} = 1$ ns, an energy crossing-threshold that defines the time zero, $E_{\mathrm{cross}} = 1$ MeV and a time zero jitter, $t_{\mathrm{jit}} = 0.5$ ns. Only EMC digits with an energy that surpasses a 12 MeV noise threshold, and CPV digits with the charge above 0.09 units are recorded. The energies in EMC are digitized in 16 bits words (which corresponds to a gain of 1.5 GeV/channel and to an overflow at 90 GeV), and the times in 12 bits words (gain 1 ps/channel). The charges in CPV are digitized in 12 bits words (gain of 0.001 units/channel and overflow at 5 units).

3   Reconstruction algorithm

The reconstruction algorithm processes the EMC and CPV digits in three steps: to produce reconstructed points, track segments, and reconstructed particles. The first step is performed separately on EMC digits and CPV digits whereas the two last steps combine the information collected by the two detectors. The particle identification can take into account additional information from the global tracking in ALICE. The particle identification could in principle take into account additional information from the global tracking in ALICE. This possibility is however not yet implemented in the PHOS reconstruction algorithm.

3.1   Clustering

The algorithm clusters neighboring digits, taken from a list ordered according to the digits location, to form reconstructed points. Two modules or cells are declared neighbors if they have a common edge or a common corner. Any EMC digit with an energy above a threshold selected above the energy deposited by minimum ionizing particles is considered as a seed of a new cluster. Clusters with several local maxims, due in general to overlapping showers, are unfolded following the algorithm described in [1]. A local maximum is defined as a digit in the cluster with an energy which differs from the energy of surrounding digits by more than a value of $E_{\mathrm{th}}^{\mathrm{lm}} = 30$ MeV. The fitting procedure takes into account the measured electromagnetic-shower profile. Such clusters are split into a set of reconstructed points with one local maximum, and the digits energy is shared in proportion given by the fitting result.

The energy E and the position of the clusters in (x, z)-plane of the module reference frame, are calculated respectively as the sum of the digit energies e_i, and the center of

gravity with a logarithmic weight:

$$\bar{s} = \frac{\displaystyle\sum_{\text{digits}} s_i w_i}{\displaystyle\sum_{\text{digits}} w_i}, \tag{1}$$

where $\bar{s}$, either $\bar{x}$ or $\bar{z}$, is the coordinate of the cluster center-of-gravity, s_i, either x_i or z_i is the coordinate of the digit and the sum extends over all digits forming the cluster. The weight w_i is defined by:

$$w_i = \max\left[0, p + \log\left(\frac{e_i}{E}\right)\right], \tag{2}$$

where e_i is the digits energy and p is a parameter which value has been empirically determined (4.5 for EMC and 4.0 for CPV). Since the edges of the crystals in a module (except for the central crystal) are not parallel to the momentum direction of particles emerging from the interaction vertex, the center of gravity of EMC clusters with the energy E is further corrected for the incidence direction, (θ, ϕ), of the primary particle:

$$
\begin{aligned}
x' &= x - (A + B \log E)\sin\phi\,, \\
z' &= z - (A + B \log E)\cos\theta\,,
\end{aligned}
\tag{3}
$$

where the parameters a and b have been determined empirically from simulation (see Eq. (8)).

Clusters in EMC are characterized by the digits multiplicity (Fig. 2), which is a function of the particle type, energy and selected digits threshold.
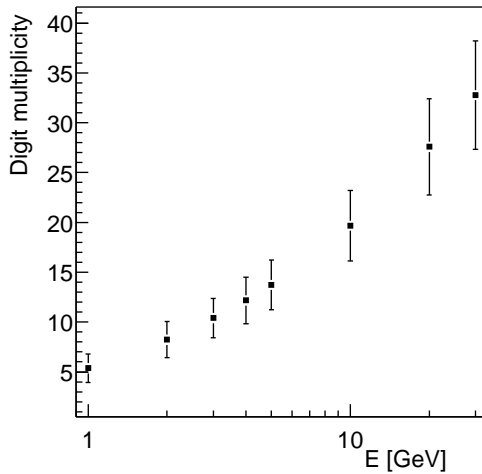

Figure 2: Digits multiplicity of EMC clusters from simulated mono-energetic photons with energies between 1 and 30 GeV. The error bars indicate the width (r.m.s.) of the multiplicity distribution.

Few additional parameters that characterize the shape of the clusters are calculated:

- The lateral dispersion, d, in the (x,z) plane measured on the surface of EMC:

$$d = \frac{\sum\limits_{\text{digits}} w_i \left[(x_i - x)^2 + (z_i - z)^2 \right]}{\sum\limits_{\text{digits}} w_i} \ .$$

- The shape of the surface, intersection of the cone containing the shower with the front plane of the calorimeter (Fig. 3.1). This surface can be expressed in terms of the covariance matrix:

$$S = \begin{pmatrix} s_{xx} & s_{zx} \\ s_{xz} & s_{zz} \end{pmatrix} , \tag{4}$$

where

$$s_{xx} = \langle (x - \bar{x})^2 \rangle \qquad = \frac{\sum\limits_{\text{digits}} w_i x_i^2}{\sum\limits_{\text{digits}} w_i} - \left(\frac{\sum\limits_{\text{digits}} w_i x_i}{\sum\limits_{\text{digits}} w_i} \right)^2 ,$$

$$s_{xz} = \langle (x - \bar{x})(z - \bar{z}) \rangle \quad = \frac{\sum\limits_{\text{digits}} w_i x_i z_i}{\sum\limits_{\text{digits}} w_i} - \frac{\sum\limits_{\text{digits}} w_i x_i \times \sum\limits_{\text{digits}} w_i z_i}{\left(\sum\limits_{\text{digits}} w_i \right)^2} ,$$

and corresponding definitions for s_{zz}, s_{zx}. Here $\langle \ \rangle$ denotes averaging with logarithmic weights w_i (Eq. (2)), $\bar{x}$ and $\bar{z}$ are the center of gravity of the cluster (Eq. (1)), (x_i, z_i) are the positions of a crystal i belonging to the cluster. Diagonalization of this covariance matrix defines the main axes of the shower surface, λ_1 and λ_2, as the square root of the eigen vectors of the covariance matrix.
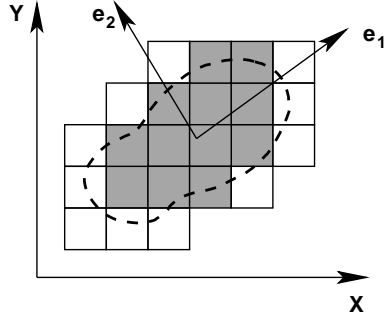

Figure 3: Example of a shower profile and its main axes e_1 and e_2.

- The sphericity parameter defined from the major axes λ_1 and λ_2:

$$\mathcal{S} = \frac{|\lambda_1 - \lambda_2|}{\lambda_1 + \lambda_2} \ .$$

- The largest fraction of the cluster energy deposited in a single crystal.

- The core energy corresponds to the summed energy of digits within a given radius

($R_{\mathrm{core}} = 3$ cm) around the largest digit. From the experimentally established shower profile, the fraction of energy deposited by an electromagnetic shower beyond this distance is less than 2%. The core energy is thus less subject to fluctuations because of background which might contribute to the cluster or because of overlapping showers.

- The time of the cluster is selected as the shortest time among the digits making the cluster.

The CPV cluster is characterized by the digits multiplicity induced by a single track, and by its extension N_x and N_z, in units of a cell, along the x and z directions in the detector reference system. These values (Fig. 4) were measured experimentally during in-beam tests [3], and the reconstruction procedure was tuned to coincide with the experimental data.
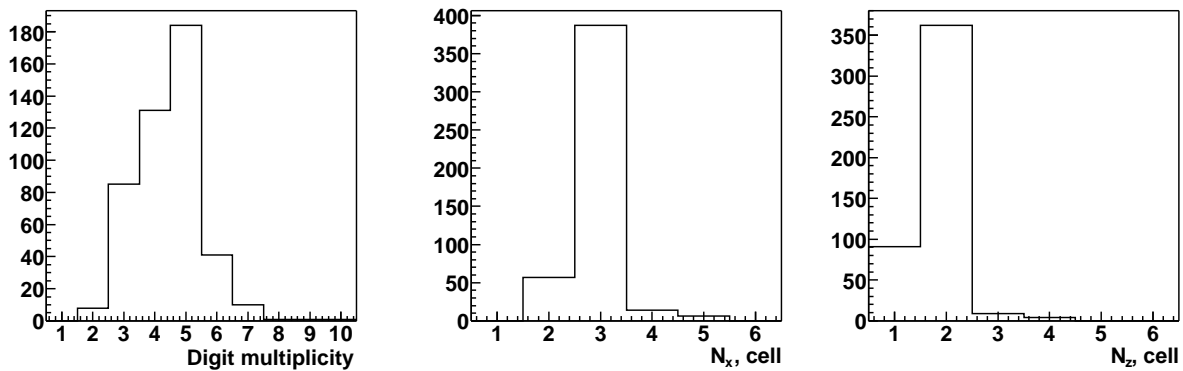

Figure 4: Digit multiplicity and cluster extension N_x and N_z along the x and z directions of the CPV cluster generated by a single charged track.

3.2 Construction of track segments

A track segment in PHOS is made up by at most two reconstructed points, one in CPV and one in EMC. First the algorithm searches for all possible pairs that are distant by less than a given distance ($d_{\mathrm{th}}^{\mathrm{link}} = 10$ cm). For a given EMC reconstructed point, the associated track segment is defined either as the pair including the considered EMC reconstructed point and the closest CPV reconstructed point among all possible pairs, or the EMC reconstructed points alone. A CPV reconstructed point can only be used once in a track segment.

3.3 Particle identification

Every track segment constitutes the seed of a reconstructed particle. Its energy is taken as the energy of the EMC reconstructed point and its momentum is taken either by the

direction passing through the EMC reconstructed point and the CPV reconstructed point or the direction passing through the EMC reconstructed point and the interaction vertex, depending on the number of reconstructed points that constitute the track segment. The type of the particle is determined following the measured parameters which characterize the track segment. Three criteria are used to identify particles: i) the Time of Flight (time elapsed between the time of the interaction and the impact of the particle on the calorimeter); ii) the charged particle rejection with the CPV and EMC; and iii) the shape of the shower that develops the particle in the calorimeter. The details on the particle identification and several identification methods will be discussed from Sec. 6 to 9.

Alternative identification methods to the ones discussed in the present note have already been published: particle identification with Bayesian approach in Ref. [11]; prompt photons and photon-jet events identification with isolation criteria in Ref. [12]; and an artificial neural network approach developed mainly to differentiate hard photons from hard π^0 in Ref. [13].

The simulation, digitization and reconstruction algorithm is demonstrated in Fig. 5. It shows the event display in one EMC module represented in the module local coordinate system. The generated event (upper left) contains 5 photons with the energy between 1 and 10 GeV. The corresponding summable digits (upper right), digits (lower left) and the reconstructed particles (lower right) are calculated with the PHOS-AliRoot simulation algorithm as explained above.
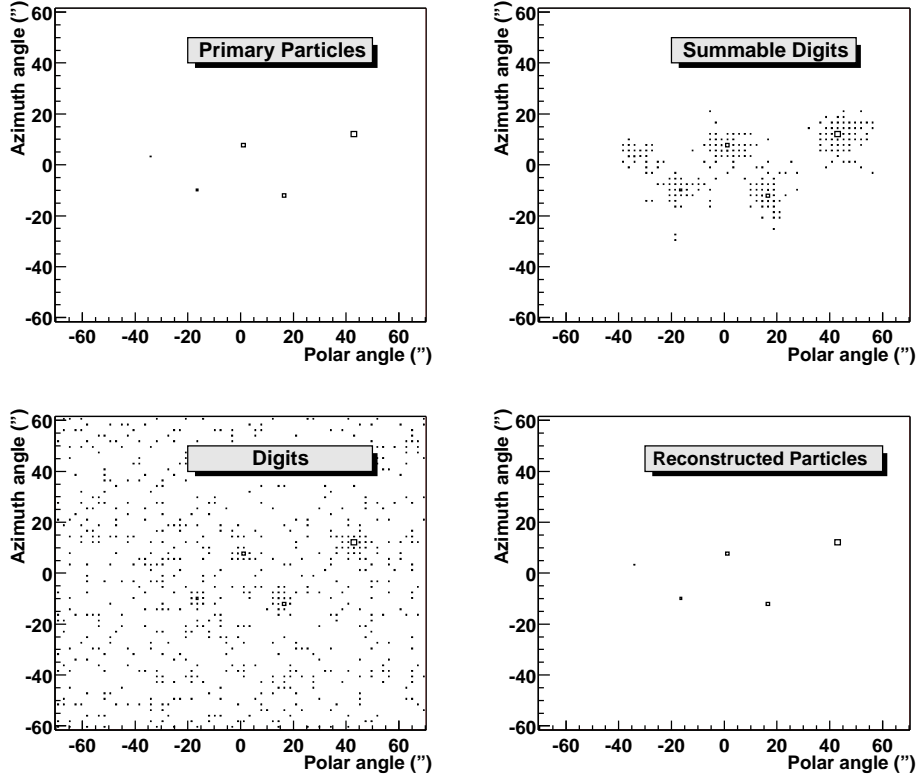
Figure 5: Event display in one EMC module demonstrating the simulation, digitization and the reconstruction algorithm.

4 Acceptance

The photon acceptance is defined as a probability that a photon, radiated from the interaction point within rapidity interval $|y| < 0.5$ and azimuth angle $0 < \phi < 2\pi$, hits PHOS. The PHOS acceptance for photons (Fig. 6) does not depend neither on their transverse momentum nor on their rapidity.

The acceptance for π^0- and η-mesons detected in the $\gamma\gamma$ decay channel is defined as a probability that both decay photons hit PHOS when the mesons are radiated from the interaction point within rapidity interval $|y| < 0.5$ and azimuth angle $0 < \phi < 2\pi$. This acceptance is small at low p_T due to the wide opening angle between the decay photons (Fig. 7). The acceptance saturates for π^0 at $pt > 20$ GeV$/c$. For η-mesons the acceptance does not reach its maximum value even at 100 GeV$/c$.

The dependences of the acceptance on p_T and y in the range $-0.13 < y < 0.13$ can be fitted by the parametric functions:

$$f(p_T) = (p_0 + p_1 p_T) \exp\left(-\frac{p_T - p_2}{p_3}\right), \tag{5}$$

$$g(y) = q_0 - q_1 y^4 \tag{6}$$
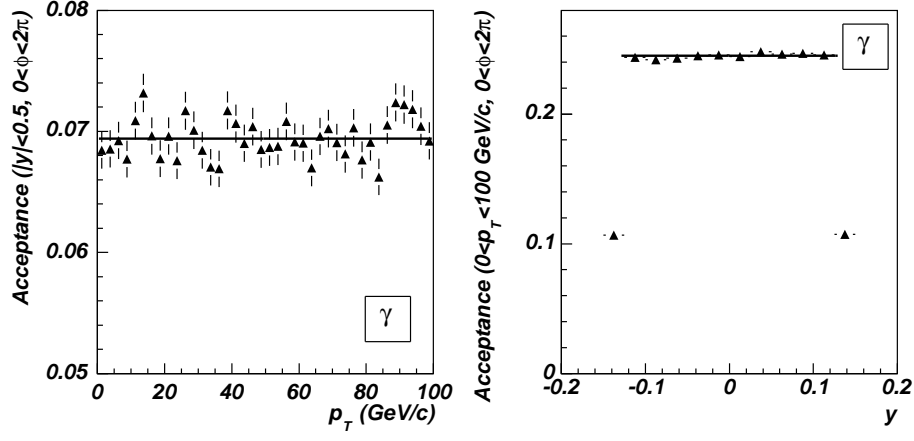
with the parameters p_i listed in Tab. 1 and Tab. 2.

11

Figure 6: Acceptance as a function of p_T (right) and y (left) for γ generated with $0 < p_T < 100$ GeV/c, $0 < \phi < 2\pi$ and $-0.5 < y < 0.5$.
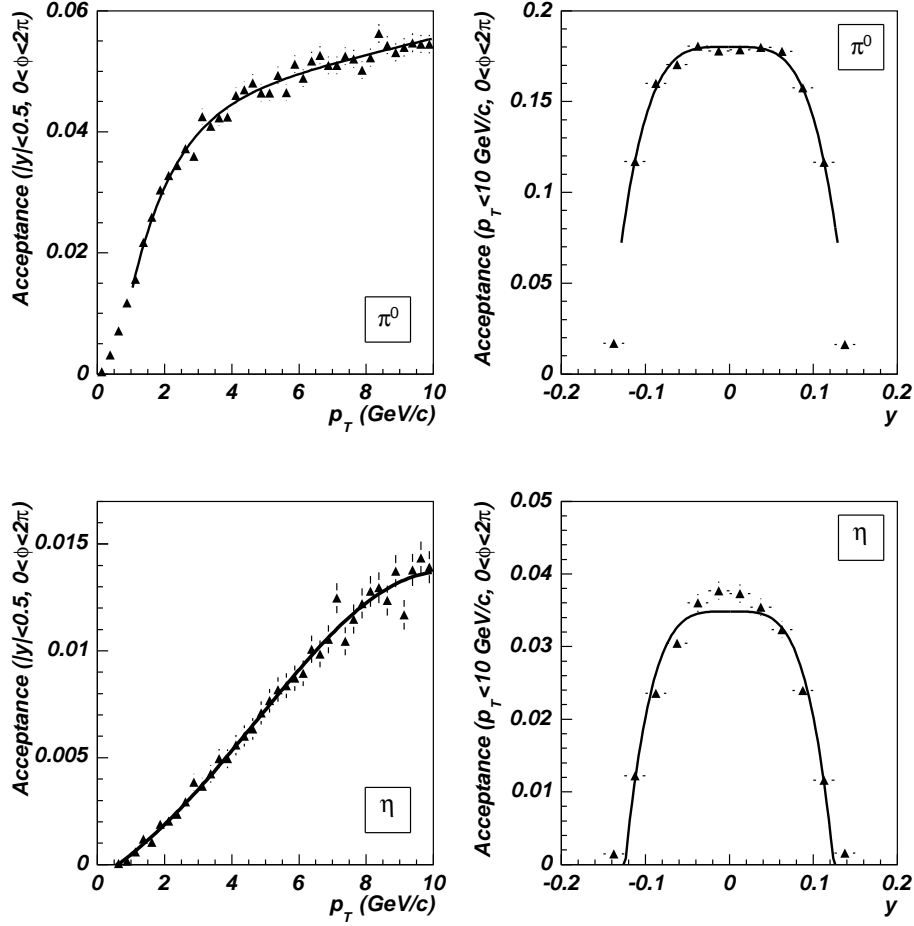

Figure 7: Acceptance as a function of p_T (right) and y (left) for low p_T π^0 (up) and η (down). The particles have been generated with $0 < p_T < 10$ GeV/c, $0 < \phi < 2\pi$ and $-0.5 < y < 0.5$.
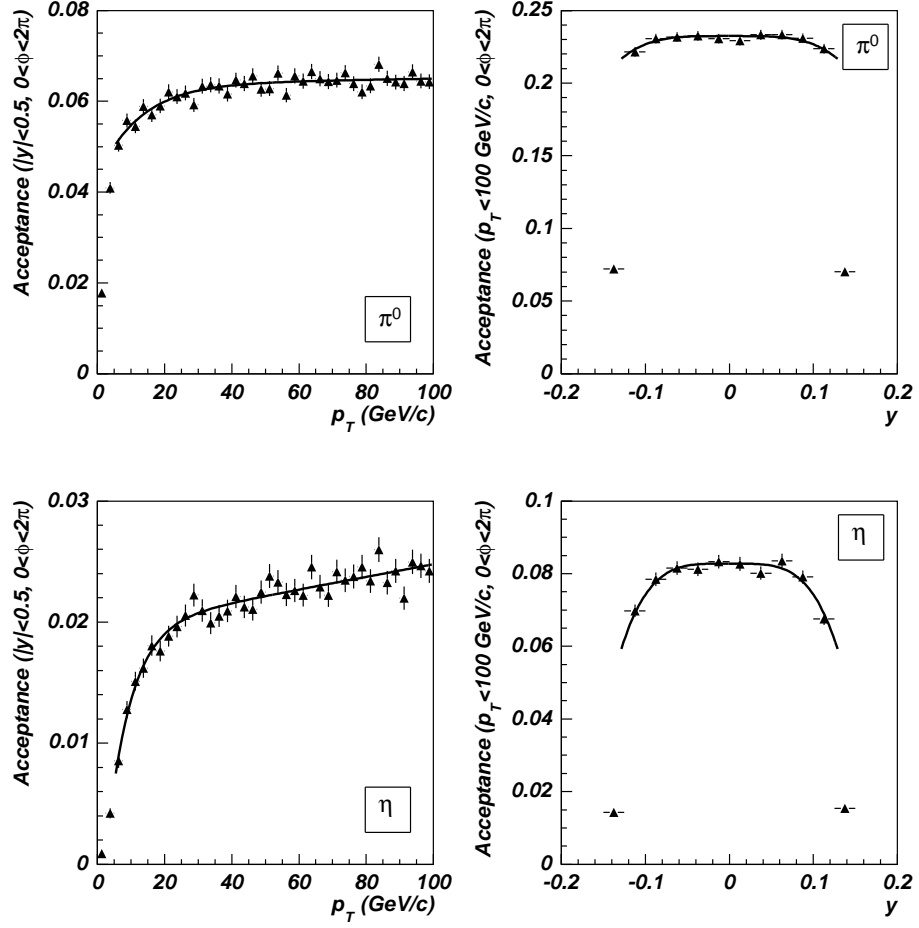
Figure 8: Acceptance as a function of p_T (right) and y (left) for high p_T π^0 (up) and η (down) mesons. The particles have been generated with $0 < p_T < 100$ GeV/c,$0 < \phi < 2\pi$ and $-0.5 < y < 0.5$.

Acc. vs. p_T	p_0	p_1	p_2	p_3
γ ($p_T < 100$ GeV/c)	0.0694±0.0002			
π^0 ($p_T < 10$ GeV/c)	0.042±0.002	0.0013±0.0003	0.55±0.07	1.25±0.16
π^0 ($p_T < 100$ GeV/c)	0.064±0.002	0.000012±0.000027	-14±6	12±4
η ($p_T < 10$ GeV/c)	0.002±0.002	0.00131±0.00015	0.75±0.07	2.3±0.9
η ($p_T < 100$ GeV/c)	0.0196±0.0007	0.000052±0.000010	2.2±0.8	86.0±9.0

Table 1: Parameters of the function $f(p_T)$ (5) which describes the acceptance dependence with p_T for γ's, π^0's and η's.

Acc. vs.y	q_0	q_1
γ ($p_T < 100$ GeV/c)	0.2451±0.0009	
π^0 ($p_T < 10$ GeV/c)	0.1801±0.0011	393.0±13.0
π^0 ($p_T < 100$ GeV/c)	0.2324±0.0013	57.0±17.0
η ($p_T < 10$ GeV/c)	0.0348±0.0005	146.0±4.0
η ($p_T < 100$ GeV/c)	0.0828±0.0008	86.0±9.0

Table 2: Parameters of the function $g(y)$ (6) which describes the acceptance dependence with y for γ's, π^0's and η's.

The PHOS installation schedule foresees the possibility to install the detector gradually, when for the first ALICE run only one module will be installed with increasing the number of modules by one in the following runs. According to this schedule, the acceptance of the PHOS detector with 1, 2 and 3 modules were studied compared to all the 5 modules. Acceptance of such reduced PHOS geometry to single photons is simply proportional to the number of modules. The same effect is expected for high-p_T π^0's. Neutral mesons at lower p_T will be more affected by the reduced geometry, and the optimization of the relative modules position is needed in this case. Fig.9 shows the PHOS acceptance to π^0-meson in the $\gamma\gamma$-decay mode with one and two PHOS modules installed (left) and with three modules (right), normalized to the total 5-module geometry. Solid lines at the levels 0.2, 0.4 and 0.6 indicate pure detector surface reduction for 1, 2 and 3 modules. Adjacent module installation (black markers) as well as installation with gaps between modules (white markers) are studied. More reduction of the π^0-acceptance in the PHOS geometry with gaps between the modules is observed at low $p_T < 3$ GeV/c. The acceptance of η-meson in the $\gamma\gamma$-decay mode for the reduced PHOS geometry is shown in Fig.10 with the same meaning of the markers as for π^0. The suppression of the acceptance for the module installation with gaps between them is more profound at low p_T up to 15 GeV/c. From these studied the conclusion can be drawn that in the case of reduced PHOS geometry in the first ALICE runs all available modules should be installed adjacently to avoid the acceptance loss.
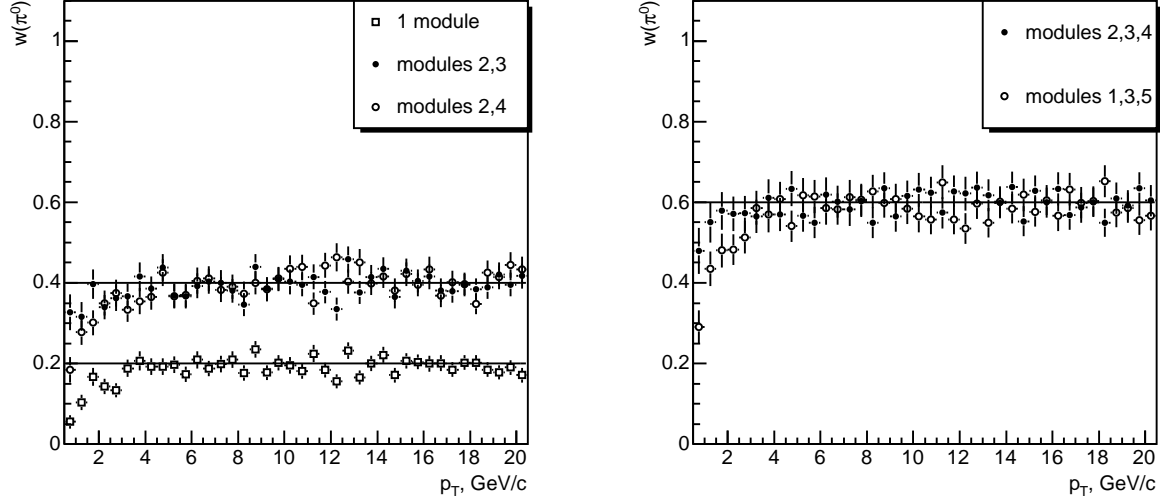
Figure 9: Efficiency of $\pi^0 \to \gamma\gamma$ detection with one PHOS module and with two modules positioned adjacently or with one-module gap (left) and the same efficiency for 3 modules positioned adjacently or with gaps (right). Efficiencies are normalized for 5-module efficiency. Solid lines at $w = 0.2, 0.4, 0.6$ shows the reduction of the detector surface with 1, 2 and 3 modules vs all 5 modules.
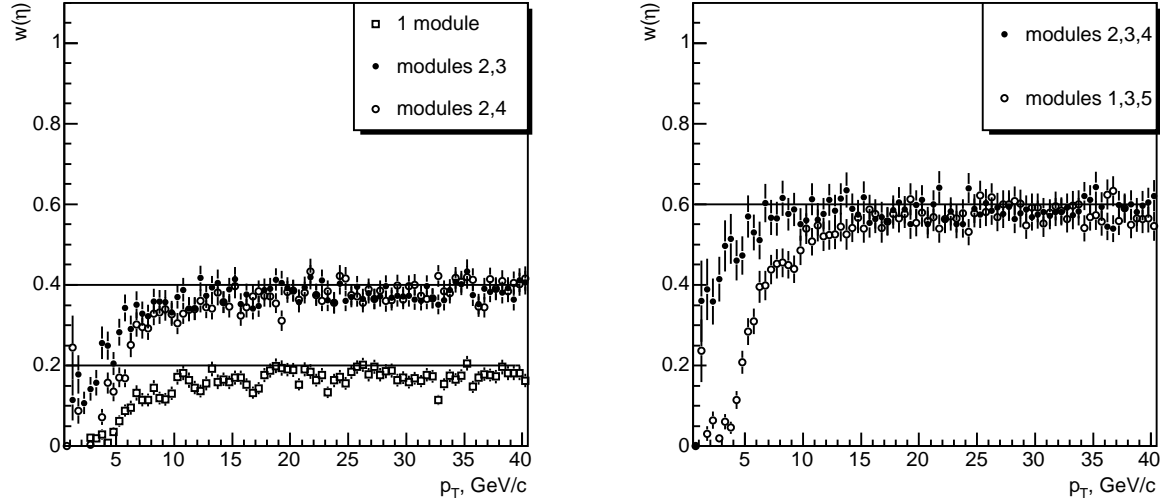

Figure 10: Efficiency of $\eta \to \gamma\gamma$ detection with one PHOS module and with two modules positioned adjacently or with one-module gap (left) and the same efficiency for 3 modules positioned adjacently or with gaps (right). Efficiencies are normalized for 5-module efficiency. Solid lines at $w = 0.2, 0.4, 0.6$ shows the reduction of the detector surface with 1, 2 and 3 modules vs all 5 modules.

15

5 Intrinsic performances

We shall now discuss the response functions of the EMC and CPV subdetectors of PHOS.

5.1 EMC performance

5.1.1 Response to electromagnetic particles

The parameters that describe the response of the EMC spectrometer and play the most important role for photon identification are the energy, the position and the time-of-flight resolutions. The energy resolution depends on the ability of the spectrometer to collect most of the energy in the electromagnetic shower, the scintillation efficiency and the light transport through the crystal, the APD photo efficiency and photo-electron gain-factor. The position resolution depends on the segmentation of the spectrometer and on the energy resolution of the individual EMC crystals.

5.1.2 Energy Resolution

The parameters of the simulation were tuned to match the calculated response function to measurements performed with electron beams of energy ranging from 0.6 to 4.5 GeV. The central module of an array of 3×3 crystals was irradiated. The energy resolution was determined from the total energy, E, collected in the array. The resulting resolution, σ/E, was compared to the one obtained by the simulation performed in exactly the same conditions as the experiment. The following parametrization was adjusted to the experimental resolution:

$$\frac{\sigma}{E} = \sqrt{\frac{a^2}{E^2} + \frac{b^2}{E} + c^2}\,, \tag{7}$$

where E is in units of GeV, a represents the contribution of the electronic noise, b the stochastic term, and c the constant term. The values of the three parameters a, b and c are determined by the simulation parameters (Section 2), while the stochastic term b depends also on the clustering algorithm parameters (Sec. 3.1). The fitted values of these parameters are summarized in Table 3. The experimental energy resolution of a 3×3 PbWO$_4$ array for electrons of energy between 0.6 to 120 GeV is compared in Fig. 11 with the simulated resolution for photons.

Switching from the static clustering, i.e. , summing the energy deposited in 3×3 array, to the dynamic clustering as in the reconstruction algorithm (see Sec. 3.1), the resulting resolution is slightly improved (see Table 3) through a lower value of the stochastic term.

The response (Fig. 12) to mono-energetic photons, with energies ranging from 0.6 to 100 GeV, impinging on the center of a PHOS block indicate that, for photon energies larger than 10 GeV, on average close to 94% of the photon energy is contained in the cluster found by the reconstruction algorithm. The parameters of the function which
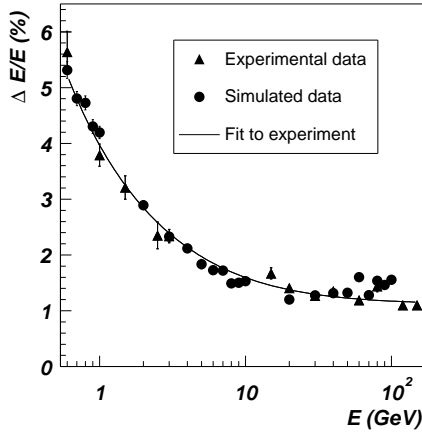
16

Figure 11: Energy resolution of a 3 × 3 PbWO$_4$ array measured in response to mono energetic electrons (▲) or calculated with simulations of mono energetic photons (●). The continuous line represents the result of the fit of Eq. (7) to the experimental data.
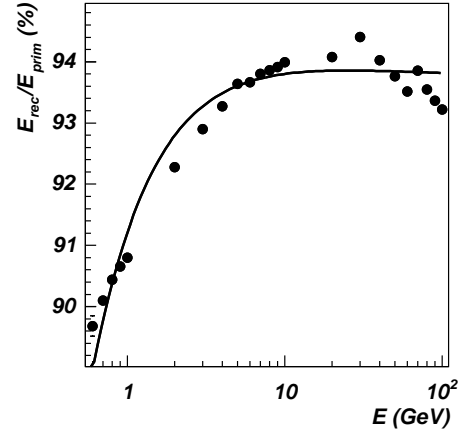
Figure 12: Fraction of the energy contained in the cluster obtained by the reconstruction algorithm for simulated mono-energetic photons (points). The line is a fit to the points by the equation $p_0/E + p_1/\sqrt{E} + p_2$.

	a (GeV)	b (GeV$^{1/2}$)	c
electron beam	0.022	0.028	0.013
static reconstruction	0.014±0.03	0.0365±0.0012	0.0067±0.0010
dynamic reconstruction (0.6-10 GeV)	0.017±0.002	0.0334±0.0013	0.0071±0.0010
simulation dynamic (0.6-100 GeV)	0.0255±0.0011	0.0272±0.0010	0.01290±0.00017

Table 3: Parameters obtained by adjusting Eq. (7) to the resolution of the measured energy collected in 3 × 3 array of EMC crystals upon the impact of mono-energetic electrons (0.6 to 4.5 GeV) and of the calculated energy from simulations of mono energetic photons (0.6 to 10 GeV or 0.6 to 100 GeV) performed in identical condition. In the static reconstruction the energy is collected in the 3 × 3 array of neighboring detector whereas in the dynamic reconstruction the standard clustering method is applied.

describes the energy resolution are reported in Table 3. At high photon energies (larger than 10 GeV) the constant term dominates and the resolution remains almost constant and equal to 1.3%.

We conclude from this study that photons can be measured in good conditions up to energies of the order of 100 GeV where the yield (estimated by considering the LHC running conditions and expected cross sections extrapolated from systematics [4]) will reach the limit of statistical significance.

5.1.3 Position Resolution

The impact position on PHOS, transverse (x) and longitudinal (z) to the beam direction, is reconstructed, as described in Sec. 3.1, by calculating the position of the center of

gravity of the reconstructed cluster. This position is further corrected for the incidence direction of the impinging photon according to Eq. (3). The test beam measurements were extended to verify the incidence on the position resolution by tilting the array of EMC modules by $\alpha = 0, 3, 6$ and $9°$.

Before applying the position correction (3), the shift of the reconstructed point with respect to the photon impact onto the EMC surface is simulated for several incidence angles and for several photon energies. Figure 13 shows the difference between the re-
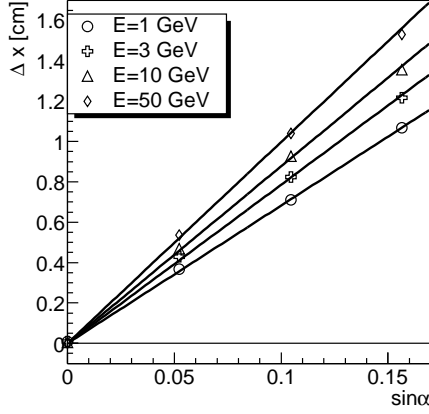
Figure 13: Difference between the reconstructed point position ($x_{\rm rec}$) and the impact coordinate ($x_{\rm in}$) on a PHOS modules versus the $\sin \alpha$ for incidence angle $\alpha = 0, 3, 6, 9°$ and for the photon energies 1, 3, 10 and 50 GeV.
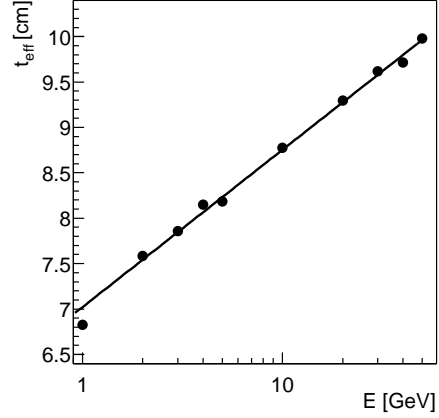
Figure 14: Dependence with photon energy of the effective maximum depth at which the shower develops in EMC crystals.

constructed point ($x_{\rm rec}$) and the impact coordinate ($x_{\rm in}$) versus the sinus of the incidence angle for various photon energies. The linear dependence with $\sin \alpha$ of the shift $x_{\rm rec} - x_{\rm in}$ is parametrized as:

$$x_{\rm rec} - x_{\rm in} = t_{\rm eff} \sin \alpha \, ,$$

where $t_{\rm eff}$ is the effective maximum depth at which the shower develops in the crystal for inclined photon tracks. Its energy dependence (Fig. 14) has been studied for photon energies from 1 to 50 GeV and is described by the function

$$t_{\rm eff} = A + B \log E \, ,$$

where the photon energy E is measured in GeV and parameters A and B are equal to

$$A = 7.02 \pm 0.04 \, , \quad B = 0.75 \pm 0.01 \, . \tag{8}$$

The position of the reconstructed points is corrected for this effect according to Eq. (3).

The width of the $x_{\rm rec} - x_{\rm in}$ distribution defines the spatial resolution. It was studied

18

(Fig. 15) for several incidence angles and photon energies. The better position resolution obtained when the photon energy increases is mostly the consequence of the increasing digit multiplicity and thus a more accurate determination of the center of gravity. The position resolution strongly depends on the incidence angle.

The function,

$$\sigma_{x,z} = \sqrt{A_{x,z}^2 + \frac{B_{x,z}^2}{E}}, \tag{9}$$

was adjusted to the experimentally measured position resolution of electrons. These results were then compared to simulations where photons from the interaction vertex illuminate entirely a PHOS module, i.e. make an incidence angle with the direction perpendicular to the surface of the EMC modules continuously distributed between 0 and 8.75°. The resolution calculated from the simulated data compares with the experimental results and is intermediate between the values obtained for 0° and 13° incidence angle. The parameters obtained by fitting Eq. (9) to the position resolution obtained for photons between 1 and 50 GeV (Fig. 15) for different incidence angles are reported in Table 4.
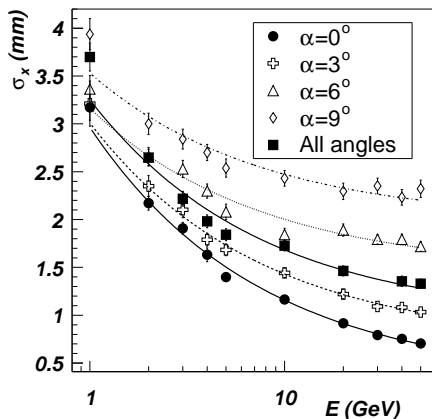

Figure 15: Position resolution versus the photon energy for the incidence angles on a PHOS module $\alpha = 0, 3, 6$ and 9° and the average for all possible incidence in the ALICE layout

α, degree	A_x, cm	B_x, cm GeV$^{1/2}$
0°	0.032	0.264
3°	0.070	0.231
6°	0.147	0.170
9°	0.198	0.155
all angles	0.096	0.229

Table 4: Parameters A_x and B_x of Eq. (9) for the incidence angles $\alpha = 0, 3, 6$ and 9° as well as for all possible incidence angles.

5.1.4 Time of flight

Presently, there exists no measurement of the time of flight (TOF) and we base our study exclusively on simulations. The resolution of TOF depends on the jitter in the time pickup for the start (the trigger) and the stop signal (the time from the EMC crystal). In our

simulations, we have neglected the jitter on the start time. With the guess made on the timing parameters a resolution of 500 ps can be achieved. This value compares well with, for example, the one achieved with the PHENIX calorimeter [5].
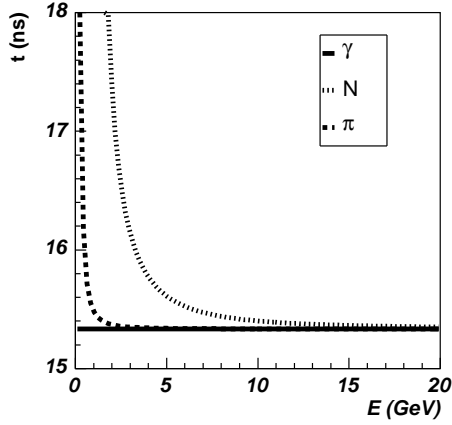

Figure 16: Time of flight of photons, π-mesons and nucleons from the interaction point to the PHOS surface versus particle energy.

The TOF resolution required to discriminate photons (and electrons) from massive particles can be deduced from Fig. 16.

Applying the TOF criterion to identify photons will mainly reject the heaviest particles with an efficiency depending on the final TOF resolution. This is illustrated by the spectra of identified photons (Fig. 17) with the changing neutron and anti-neutron contamination as the TOF resolution changes.
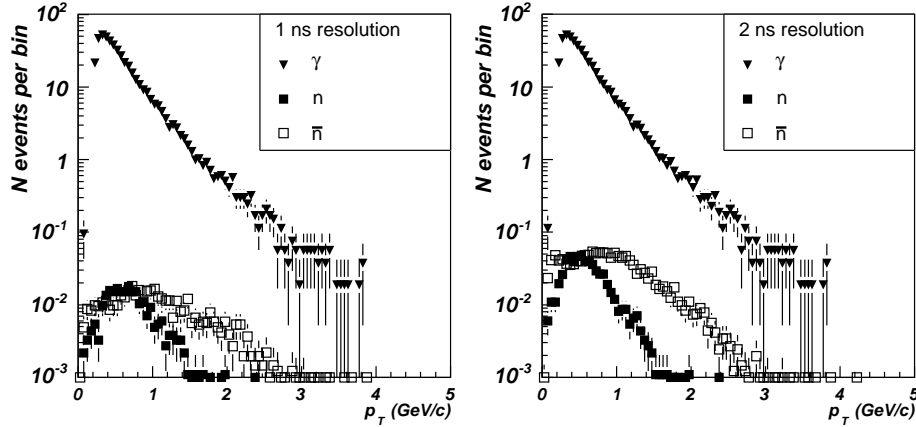

Figure 17: Spectra of photons (▼), neutrons (■) and anti-neutrons (□) generated by central Pb-Pb HIJING [6] events, identified as low purity photons by the TOF criterion (see Sec. 6.1.2) for time resolutions of 1 and 2 ns.

5.1.5 Response to hadrons

Hadrons produced at LHC energies enter PHOS with minimum-ionizing energies. They therefore deposit in EMC a constant energy that only depends on the amount of traversed

material. The average value of the energy deposited in a single EMC module has been estimated from GEANT3 simulations of charged pions, with energy between 0.5 and 10 GeV, emitted from the ALICE vertex, and irradiating one EMC module. It is found (Fig. 18) equal to 227±3 GeV. However, a fraction (51% of the hadrons deposit an energy larger than 350 MeV) of the hadrons trigger a shower inside the calorimeter, through hadron-nucleus interactions.
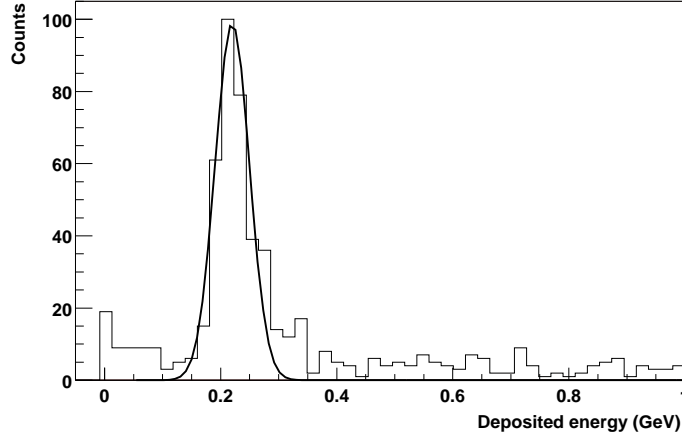

Figure 18: Energy deposited, as calculated from a GEANT3 simulation, in a single EMC module by charged pions of energy between 0.5 and 10 GeV, emitted from the ALICE vertex, and irradiating one EMC block.

With anti-protons and anti-neutrons, the situation is particular, since these particles annihilate inside the crystals and may deposit more energy than protons and neutrons. The annihilation of anti-nucleons produces most likely charged pions, we do not expect that anti-nucleons deposit the 2 GeV corresponding to the mass of the two annihilated baryons. Moreover, since anti-nucleons travel a given distance before annihilating (the nuclear interaction length in $PbWO_4$ is 19.5 cm), the impact position obtained from the clustering algorithm for oblique tracks is different from the true impact position. This effect deteriorates the identification of anti-protons by correlating hits in the CPV and EMC.

The response of PHOS to hadrons depends on several factors like the hadron type and energy and the detector occupancy by other particles. The spectrum of primary hadrons can be obtained by unfolding the spectrum of reconstructed hadrons with the help of the reconstructed energy E_{rec} versus the primary energy E_{prim}, however, this unfolding has not been done yet.

5.2 CPV performance

5.2.1 Response to ionizing particles

The CPV detector is sensitive to any particle which triggers an ionization process in the CPV gas volume. Therefore it will detect charged particles with almost any momentum. The only parameter which defines the response of the CPV is the position resolution of the charged track passing through the detector.

5.2.2 Position Resolution

The impact position on CPV is reconstructed directly as the center of gravity of the cluster made of neighboring pads with non-zero deposited energy. In-beam tests were carried out at the CERN PS accelerator with beams of different charged particles (electrons, hadron, muons) in the momentum range $1 - 5$ GeV/c [3]. To measure the position resolution experimentally, a gas strip-detector (GSP) with position resolution of 60 μm was used as a reference detector. The effective spatial resolution of CPV was measured as $\sigma_x = 0.138$ cm (across the wires) and $\sigma_z = 0.154$ cm (along the wires). AliRoot simulations (Fig. 19) reproduce the coordinate resolution of the CPV.
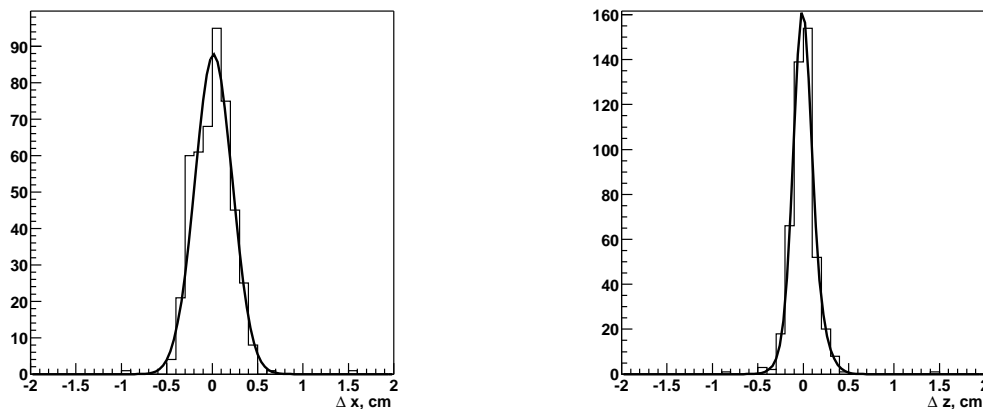

Figure 19: Difference between the exact coordinate of the charged particle impact on the CPV, and the reconstructed coordinate. The plot for the x-axis (across the anode wires) is fitted by a single Gaussian, and for the z-axis (along the anode wires) is fitted by a sum of two Gaussian [3].

5.3 Modifications in the colliding heavy-ion environment

In the high particle-multiplicity environment created in ALICE by heavy-ion collisions, the intrinsic performances, energy and position resolution, of EMC will deteriorate. By how much the performances will degrade depends obviously on the occupation of EMC, the larger the occupancy the more probable the overlapping of an electromagnetic shower and a charged particle impact, or hadronic shower. This effect has been studied by

embedding mono-energetic photons in a central heavy-ion collision event. The central event was generated using the parametrized HIJING [6] and setting the particle density at central rapidity equal to 8,000. The change in energy resolution and in the fraction of reconstructed energy are displayed in Fig. 20. Because of shower overlapping, the energy resolution is noticeably degraded, the effect being the largest for low energy photons. The new parameters fitting the energy resolution dependence with the photon energy (Eq. (7)) are as follows (cf. Tab. 3): $a = 0.00(6)$ GeV, $b = 0.0593(12)$ GeV$^{1/2}$ and $c = 0.0136(2)$.
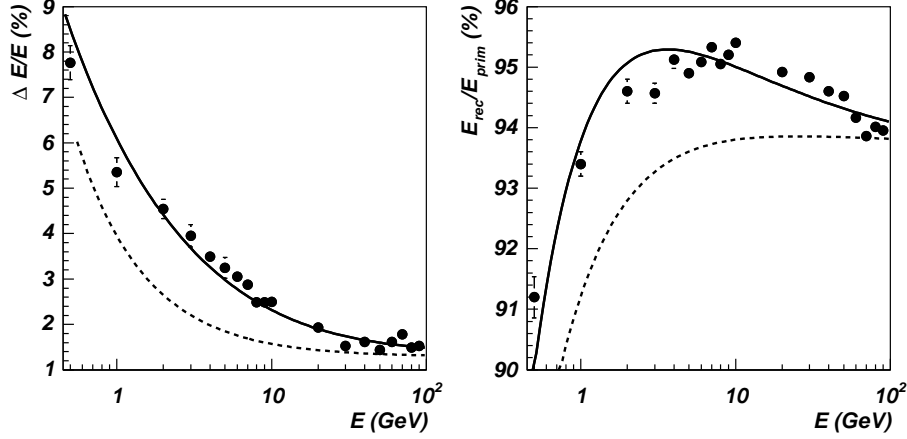
Figure 20: Energy resolution (left) and fraction of energy contained in the cluster (right) found by the reconstruction algorithm for simulated mono-energetic photons impinging on the center of a PHOS block and embedded in a central heavy-ion collision environment with charged particle density at mid-rapidity of 8,000. The dashed curves represents the values obtained for photons in a particle free environment (Figs. 11 and 12). Solid lines on the left and right figures are a fit to the points by Eq. (7) and equation $p_0/E + p_1/\sqrt{E} + p_2$, respectively.

5.4 Modifications due to the ALICE environment

The previously discussed performances will be modified when PHOS is incorporated in the ALICE experiment. Several effects will contribute to performance degradation, e.g. , conversion and scattering of photons in the material between the interaction point and PHOS and particles not originating from the vertex. The above simulations have been repeated to study the impact on the energy resolution of material in front of PHOS [7]. Writing the change in the resolution with and without material as:

$$\frac{\sigma_E^w}{\sigma_E^{wo}} = 1 + d \, ,$$

we find that the degradation d scales approximatively with two times the interaction probability: $d \sim 2P_I$, with the following relations linking interaction probability and the

material thickness, X:

$$P_\mathrm{I}^\gamma \;=\; 1 - e^{-7X/9X_0} \ \text{for photons},$$

$$P_\mathrm{I}^\mathrm{e} \;=\; 1 - e^{-X/X_0} \ \ \text{for electrons}.$$

The material budget in front of PHOS in terms of radiation length X has been studied for two ALICE geometry options. In one geometry only ITS and TPC detectors are installed between the interaction point and PHOS while in other central detectors TOF and TRD there are holes in the aperture of PHOS (so called "holes" geometry). Another geometry configuration has no holes in TOF and TRD (referred to as "no holes" geometry). The radiation length distribution of the material in front of PHOS versus the polar angle θ for these two geometries are shown in Fig.21. In the case of "holes" geometry the
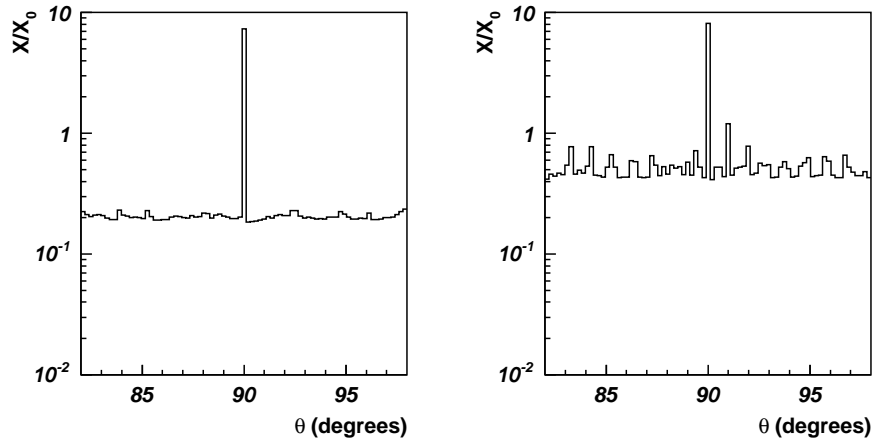
Figure 21: Radiation length of all material in front of PHOS vs polar angle θ for "holes" configuration (left) and for "no holes" (right) configurations.
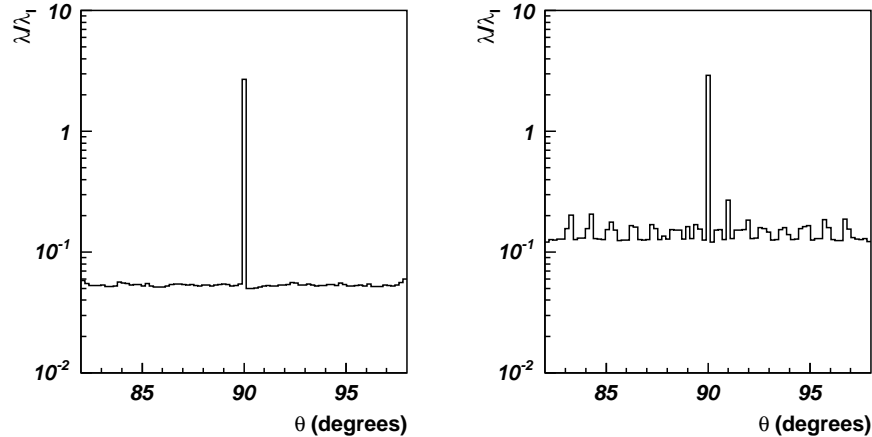

Figure 22: Nuclear absorption length of all material in front of PHOS vs polar angle θ for "holes" configuration (left) and for "no holes" (right) configurations.

average radiation length in front of PHOS is equal to $0.2X_0$ except a high peak at $\theta = 90°$ because of the TPC central electrode. With TOF and TRD installed in front of PHOS,

the average radiation length increases by a factor 2.5 and becomes $0.5X_0$ with several peaks up to $0.7X_0$ due to internal structures of TOF and TRD. Such high values will degrade the energy resolution so badly that the accuracy with which the spectrometer measures neutral mesons will be reduced by a factor of 4 [8]. Installation of TOF and TRD in the PHOS aperture also increases the nuclear absorption length by a factor of 3, from about $0.05\lambda_I$ to $0.14\lambda_I$ (Fig.22).

Installation of extra material between the interaction point and PHOS by covering the PHOS aperture by TOF and TRD deteriorates the PHOS capability to reconstruct and identify particles. The distributions of reconstructed particle multiplicity in PHOS in the most central Pb-Pb collisions ($b < 2$ fm) calculated for "holes" and "no holes" geometries (Fig.23) indicate that the average number of all reconstructed particles in PHOS (left
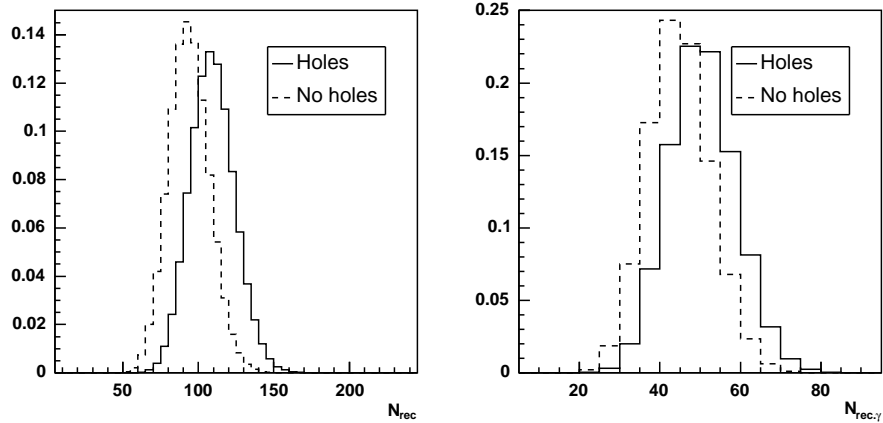

Figure 23: Distributions of all reconstructed particles number (left) and of reconstructed photons (right) in PHOS in central Pb-Pb collisions for "holes" and "no holes" configurations.

plot) is reduced due to TOF and TRD from 109 to 94 particles per event, and the average number of reconstructed and identified photons (right plot) is reduced from 51 to 45, i.e. "No holes" detector configuration leads to 12%-loss of particles in PHOS. Dependence of the reconstructed photon and π^0 spectra on transverse momentum in the central Pb-Pb collisions is shown in Figs. 24 and 25, respectively. Left plots of these figures show the p_T-spectra of reconstructed photons and π^0-mesons, and the right plots show the ratios of the reconstructed spectra with "no holes" configuration to the spectra with "holes". For high-energy photons from 10 to 40 GeV, the effect of the TRD and TOF material is similar to the one observed at lower energies as seen in Fig. 26.

From the ratios of spectra one sees that the lost of photons at $p_T > 1$ GeV/c as about 20%, and the lost of π^0 is about 40% in the "No holes" configuration.
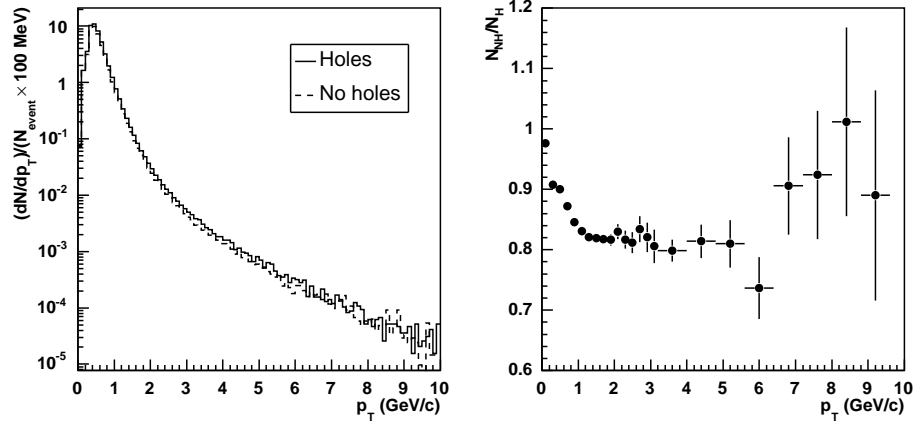
Figure 24: Left: Spectrum of reconstructed photons per one central Pb-Pb collision for "holes" and "no holes" configurations. Right: Ratio of the reconstructed photons spectrum in the "no holes" configuration to that in the "holes" configuration.
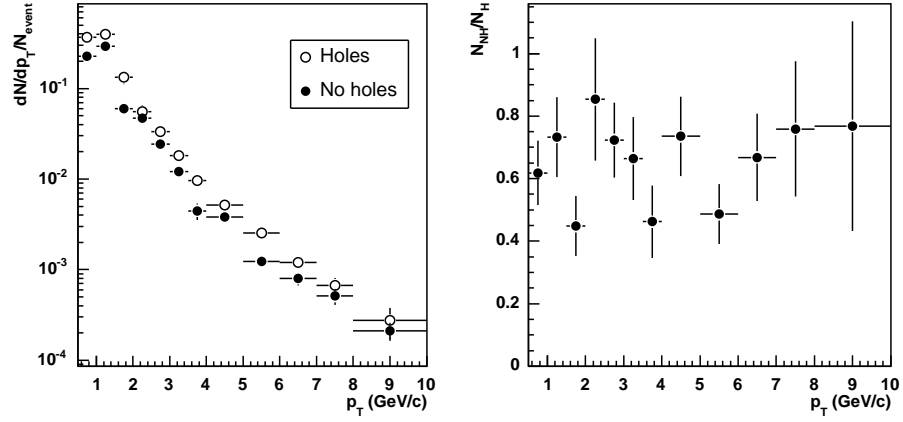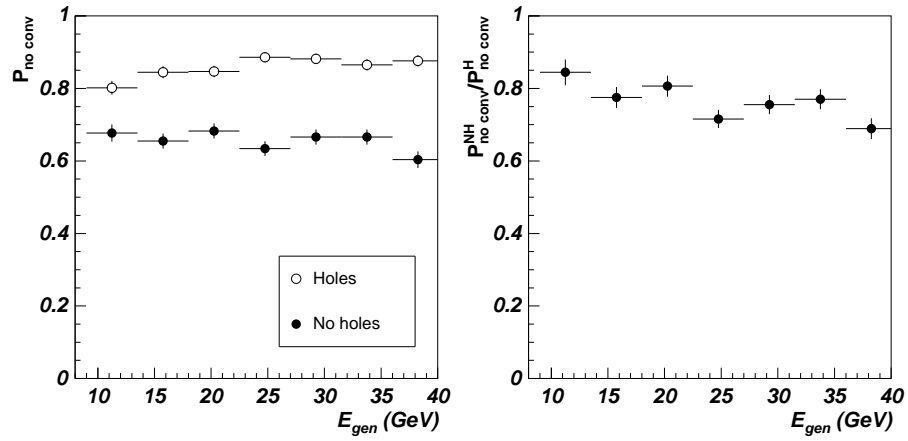

Figure 25: Left: Spectrum of reconstructed π^0-mesons per one central Pb-Pb collision for "holes" and "no holes" configurations. Right: Ratio of the reconstructed π^0 spectrum in the "no holes" configuration to that in the "holes" configuration.

Figure 26: Left frame: Probability that high-p_T photons do not convert in the material in front of PHOS calculated as the ratio of the number of photons that arrive to PHOS to the number of generated photons for the configurations with (○) and without (●) holes. Right frame: Ratio of the no conversion probability for the configurations with and without holes. Photons have been generated with energy uniformly distributed from 10 to 40 GeV.

6 Particle identification

In this section, the details of the particle identification in PHOS are discussed. Photons are identified according to three quality classes, defined with respect to efficiency and purity. The efficiency is defined as the ratio of the number of reconstructed particles identified as photons to the number of primary (generated) photons. The purity is defined as the ratio of the number of reconstructed particles identified as photons, which are indeed produced by photons, to the total number of reconstructed particles identified as photons.

6.1 Particle identification criteria

The ability of PHOS to identify particles is based in three identification criteria: time-of-flight measurement by the PHOS front-end electronics, charge particle rejection by the CPV detector and the analysis of the shower shape developed by different particles in the electromagnetic calorimeter.

6.1.1 Charged particle identification with the CPV

Showers in EMC can be initiated by photons as well as by charged particles. Electromagnetic charged particles (electrons either positrons) will produce electromagnetic showers in the calorimeter, while charged hadrons can produce hadronic showers or minimal ionizing signals. The CPV capability to identify showers produced by charged particles can be determined by matching the positions of CPV and EMC reconstructed points. The width of the distributions (Figs. 27 and 28)of the relative distance, measured within the ALICE environment, is about 1 cm, and it is larger for pions. We use this criterion to identify
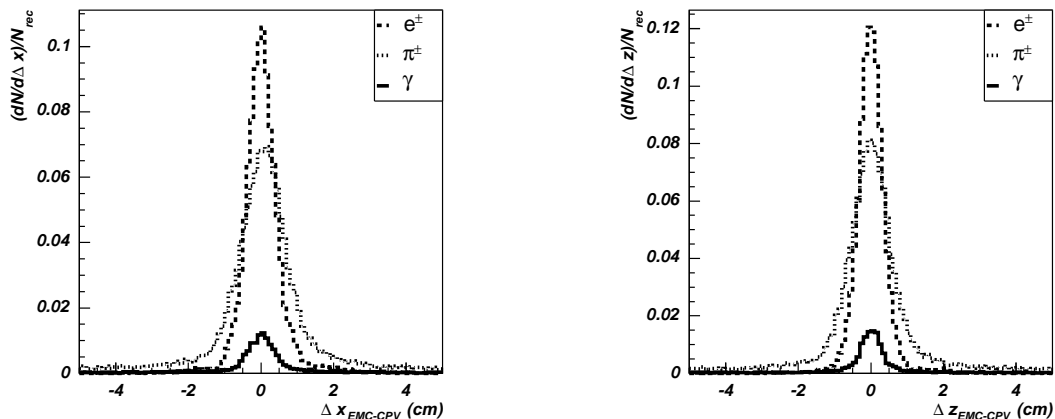

Figure 27: Distance between the EMC and the CPV reconstructed points across the beam (left) and along the beam (right). The distributions are shown for single photon (solid line), electron (dashed line) and $\pi^\pm$ (dotted line) and normalized to the number of the EMC reconstructed points. The simulations were performed within a realistic ALICE environment.
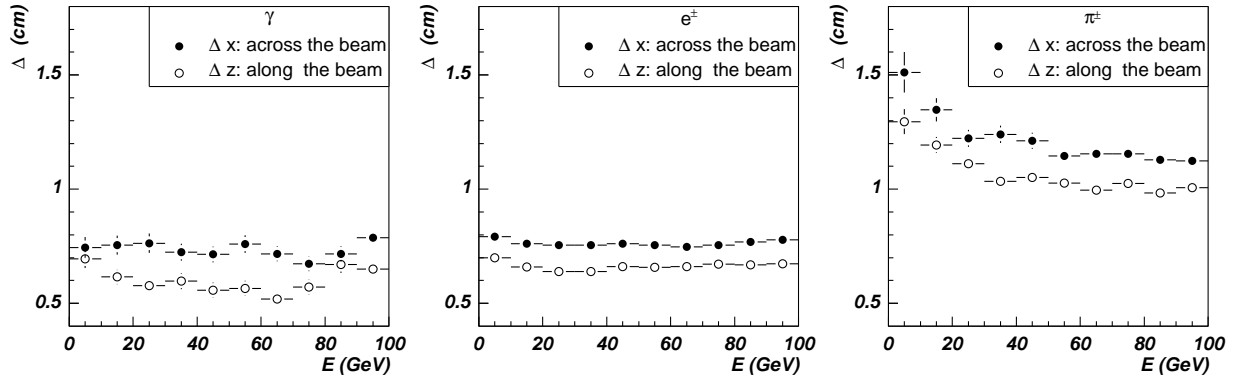
Figure 28: Widths of the distance from the EMC to the CPV hit across (●) and along the beam (○) versus particle energy for photons (left), electrons(middle) and charged pions (right). The vertical error bars indicate the Gaussian fit uncertainty.

charged particles in the ALICE environment and obtain the relevant efficiencies (Fig. 29). The probability to misidentify photons as charged particles is about 10% over the whole energy range and results from the photon conversion into e^+e^- pair in the material budget in front of PHOS. The probability of electron identification as charged particles is only about 90% because of losses due to bremsstrahlung in the material. The probability of charged pion identification as charged particles is less than that for electrons because pions which deposit the minimum ionizing energy are not recorded by EMC.
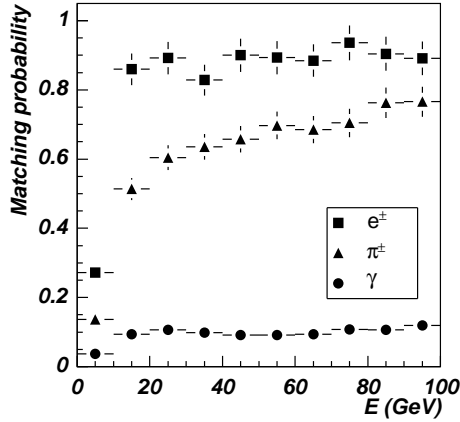

Figure 29: Probability to accept the EMC reconstructed impact point as a charged particle versus the incident particle energy for photons (●), electrons (■) and charged pions (▲).

In the reality, the situation will be different for electromagnetic particles, which deposit essentially all their energy in EMC, and hadrons, which deposit only a small fraction. Therefore what counts for hadrons is the dependence of the average CPV-EMC distance σ on the reconstructed energy (Fig. 30). This dependence in the two directions x and z can be described by the function:

$$\sigma(\Delta x, \Delta z) = a + \exp(b - Ec) \, , \tag{10}$$

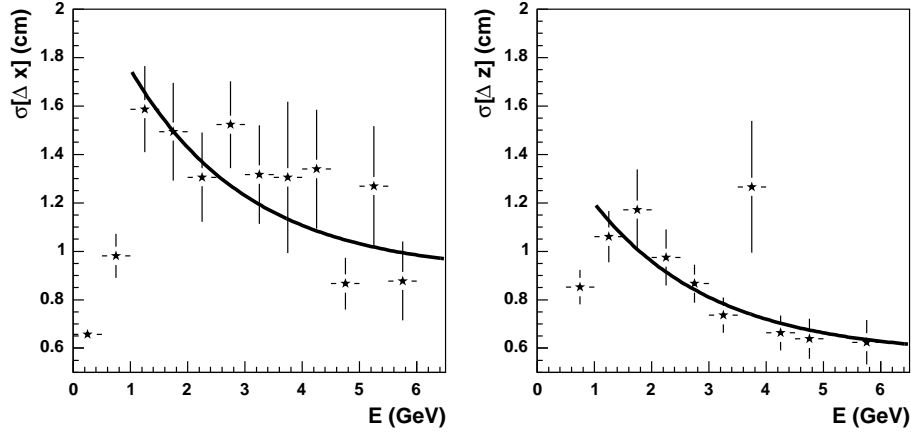where the average distance σ is measured in cm, the reconstructed energy E is expressed

Figure 30: Standard deviation of the distance between the reconstructed impact points in the CPV and EMC along the x-axis and z-axis (along the beam) for charged pions produced with a uniformly distributed energy from 0 to 100 GeV vs the reconstructed energy. The lower points between 0 and 1 GeV correspond to minimum ionizing particles which have larger energy and therefore smaller widths.

in GeV and the parameters a, b and c are equal to:

axis	a	b	c
x	0.64	0.44	0.30
z	0.54	0.14	0.42

The identification is performed using three criteria depending on the purity quality one aims to achieve. Three definitions of a neutral particle purity are introduced in the particle identification in PHOS: low, medium and high purity which identify a neutral particle if there is no matching reconstructed point in CPV within a rectangular defined by 1, 2 and 3 standard deviations, respectively. Formally the condition for a neutral particle selection is expressed by the following inequalities:

$$|x_{\text{EMC}} - x_{\text{CPV}}| > \kappa\sigma(\Delta x),$$
$$|z_{\text{EMC}} - z_{\text{CPV}}| > \kappa\sigma(\Delta z),$$
$$\kappa = 1, 2, 3\,,$$

where the factor κ defines the purity: low, medium and high respectively.

6.1.2 Slow particle rejection by time of flight

A reconstructed particle is qualified as a photon-like if its time of flight is consistent with that of a photon, i.e. 15.3 ns. Two qualities of photon-like particles are considered, high-purity (TOF < 16.5 ns) and low-purity (TOF < 17.0 ns), see Fig.16 .

	p_0	p_1	p_2	p_3
a	0.52	$8.4 \cdot 10^{-3}$	$-6 \cdot 10^{-5}$	0.23
b	0.47	$8.3 \cdot 10^{-3}$	$-5.6 \cdot 10^{-5}$	0.42
c	0.36	$1.4 \cdot 10^{-2}$	$-8 \cdot 10^{-5}$	-0.99
x_0	-0.75	$1.9 \cdot 10^{-2}$	$4 \cdot 10^{-6}$	1.49
y_0	0.91	$-3 \cdot 10^{-2}$	$1.1 \cdot 10^{-4}$	1.03

Table 5: Parameters obtained by fitting the PCA photon ellipse parameters a, b, c, x_0 and y_0 of Fig. 33 by the function $f(E) = p_0/\sqrt{E} + p_1 E + p_2 E^2 + p_3$.

6.1.3 Shower shape analysis in the PCA approach

The shower generated in the calorimeter is characterized by the following seven parameters, already defined in Sect. 3: lateral dispersion, two ellipse axes, sphericity parameter, core energy, largest fraction of energy deposited in a single crystal; and digit multiplicity of the shower. Ideally one could define selection criteria on this multidimensional surface, but that would be a tedious task with no guarantee to find the absolute minimum. A set of seven statistically independent parameters, referred to as the principal components, can be obtained by diagonalizing the covariance matrix of the original seven parameters. Thus, showers produced by different kind of particles, can be recognized in the space of the principal components within an approach known as the Principal Component Analysis (PCA) [9]. The two most significant principal components, i.e. those two components which correspond to the largest eigen values of the covariance matrix, were used to identify showers (Fig. 31) in the 2-dimensional space spanned over these two principal components.

Variable contours (Fig. 32) depending on the EMC cluster energy and on the particle identification quality one desires to achieve, have been defined. Particles inside this contour are tagged as photons, and those outside as any other particle.

These 2-dimensional distributions were fitted by a 2-dimensional Gaussian function

$$f(p_0, p_1) = \exp[-R(p_0, p_1)] \,,$$
$$R(p_0, p_1) = \left(\frac{p_0 - x_0}{a}\right)^2 + \left(\frac{p_1 - y_0}{b}\right)^2 + C\frac{(p_0 - x_0)(p_1 - y_0)}{ab} \,, \tag{11}$$

where the parameters a, b, c, x_0 and y_0 depend on the reconstructed energy. The evolution of these parameters with energy is shown in Fig. 33. Three classes of photon purity κ are defined: high, medium and low purities which correspond to the reconstructed particles occupying the areas in the (p_0, p_1) space defined by the argument R of Eq. (11):

$$R(p_0, p_1) < \kappa/2$$

with $\kappa = 1, 4, 9$ respectively, defining 1, 2 and 3 standard deviations from the shower center in the (p_0, p_1) space. These three areas are illustrated as the three ellipses in
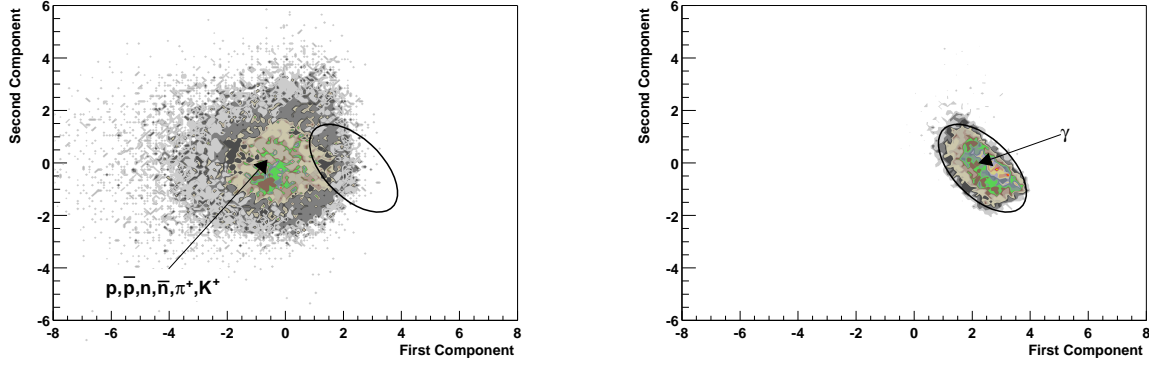
Figure 31: First and second components from the principal components analysis. The analysis was performed for single-particle events of photons (right hand side), charged pions, charged kaons, protons, anti-protons, neutrons and anti-neutrons (left hand side plot). Their transverse momentum was uniformly distributed between 0.5 and 100 GeV/c. The particles pointed in PHOS acceptance. The contour on the figure corresponds to the photon identification cut with high efficiency (95%) and low purity (79%).
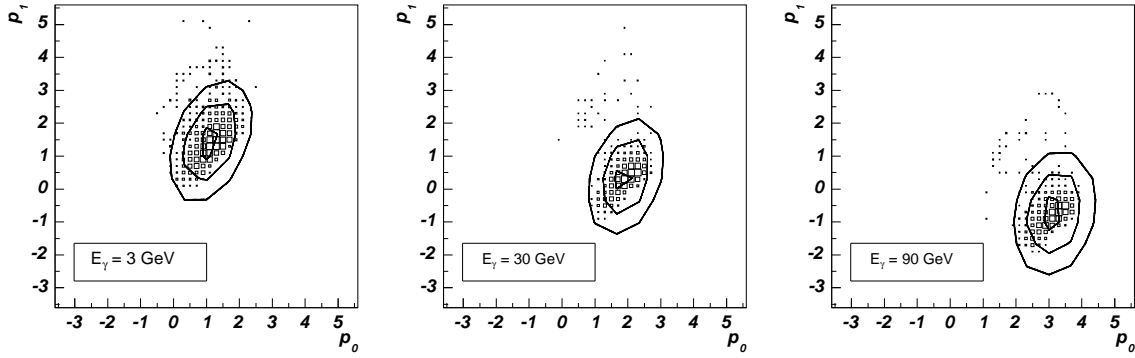

Figure 32: Photon shower distribution in the space defined by the two first principal components (p_0, p_1). Photon showers of three energies have been considered: 3, 30 and 90 GeV. The three different ellipses in each plot are the contours corresponding to high (smallest ellipse), medium and low (largest ellipse) purity.
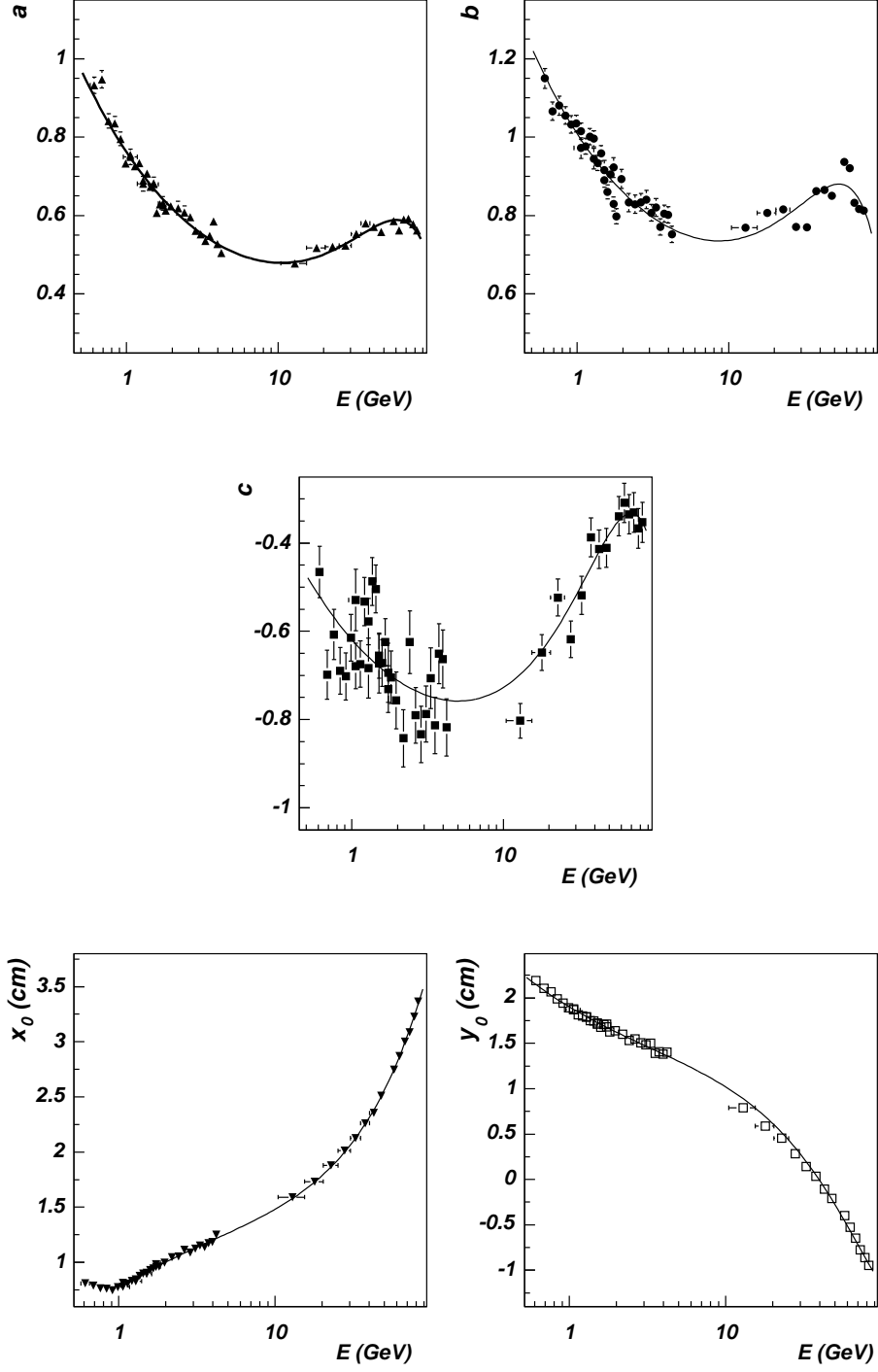
Figure 33: Parameters a, b, c, x_0 and y_0 of the PCA ellipse for photons vs reconstructed photon energy. Points were fitted by the function $f(E) = p_0/\sqrt{E} + p_1 E + p_2 E^2 + p_3$; the p_i are given in Tab. 5.
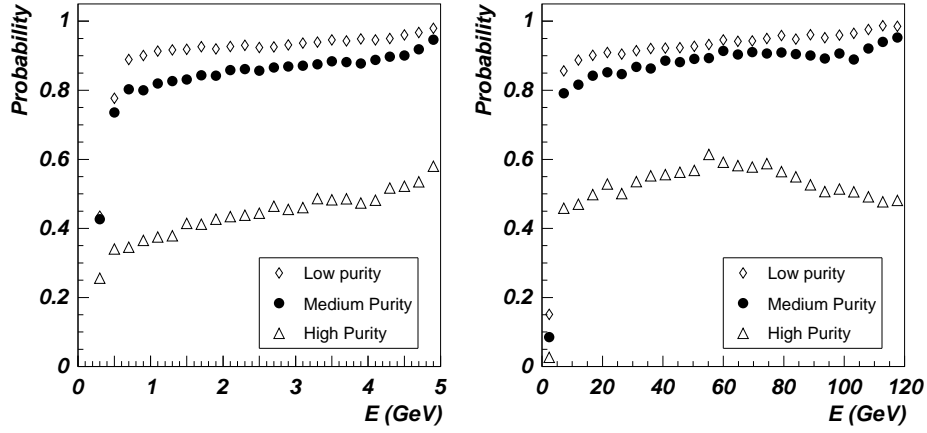
Figure 34: Photon identification probability with low (◇), medium (●) and high (△) purity levels for single photons of $E < 10$ GeV (left) and $E < 120$ GeV (right) as a function of the reconstructed photon energy.

Fig. 32.

6.2 Particle identification probabilities

6.2.1 Single photons

The identification probability is defined as the ratio of the spectrum of reconstructed particles identified as photons to the spectrum of all reconstructed particles. The three identification criteria (CPV, TOF and PCA) were applied simultaneously and the probability for three purity classes defined above were obtained[6]. These probabilities, given in Fig. 34 as a function of the energy, were calculated for photons of energy uniformly distributed in two different energy ranges: from 0.5 to 5 GeV and from 0.5 to 120 GeV. In these simulations, the other ALICE detectors were not considered.

6.2.2 Photons in a heavy-ion environment

The high occupancy of PHOS in heavy-ion collisions induces a significant number of overlapping showers. In central HIJING Pb-Pb collisions ($b < 2$ fm), about a third of the EMC reconstructed points are associated to more than one primary particle, as observed in Fig. 35. To avoid identification ambiguities in the simulations, we have assigned to each reconstructed point the primary particle that contributes with the largest fraction of energy to it.

---

[6]Low purity = TOF low purity + CPV low purity + PCA low purity.
Medium purity = TOF medium purity + CPV medium purity + PCA medium purity.
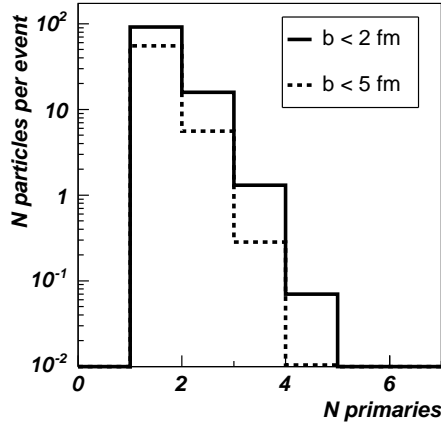High purity = TOF high purity + CPV high purity + PCA high purity.

Figure 35: Average number of reconstructed particles for central HIJING events (Pb-Pb collisions at 5.5A TeV) as a function of the number of primary particles associated with one reconstructed particle in the EMC. Two impact parameters are considered $b < 2$ fm (solid line) and $b < 5$ fm (dashed line).

Low-energy photons in a heavy-ion environment. The photon identification probability was calculated for each of the TOF, CPV and PCA criteria separately and for the three criteria combined for particles in the reconstructed energy range $0 < E < 5$ GeV. To evaluate the contamination of the identified photon spectrum, we consider charged pions, protons, neutrons and their anti-particles.

The identification probability by TOF shown in Fig. 36 indicates that TOF measurements alone cannot discriminate photons from nucleons for reconstructed energies larger than 1.5 GeV. This threshold is higher for anti-nucleons because they deposit additional energy through their annihilation. Charged π-mesons cannot be discriminated from photons for energies higher than 0.5 GeV. Concerning the CPV criterion, charged particles are efficiently discriminated from neutral particles for reconstructed energies higher than 1 GeV as illustrated in Figs. 37 and 38. Soft hadrons so are significantly deflected by the magnetic field that the distance of their impact point in CPV and EMC is sufficiently large to produce their misidentification as photons. We observe that neutral particle identification probabilities are well below 100 %. This is due to a mismatch in the tracking between the CPV and the EMC produced by the HIC environment. This effect increases with the particle multiplicity of the event; for $b < 2$ fm the probability of misidentifying neutral particles is about a 10 % worse than for $b < 5$ fm. The probability of identifying photons by the PCA criterion shows a minimum at about 1.5 GeV; hadrons are misidentified as photons with a high probability for reconstructed energies lower than 0.5 GeV but for higher energies the probability is small as seen in Figs. 39 and 40. The PCA identification criterion is efficient for reconstructed energies $E > 1$ GeV, although a strong dependence of the identification probability with the particle multiplicity is observed. The shape of this probability is explained below.
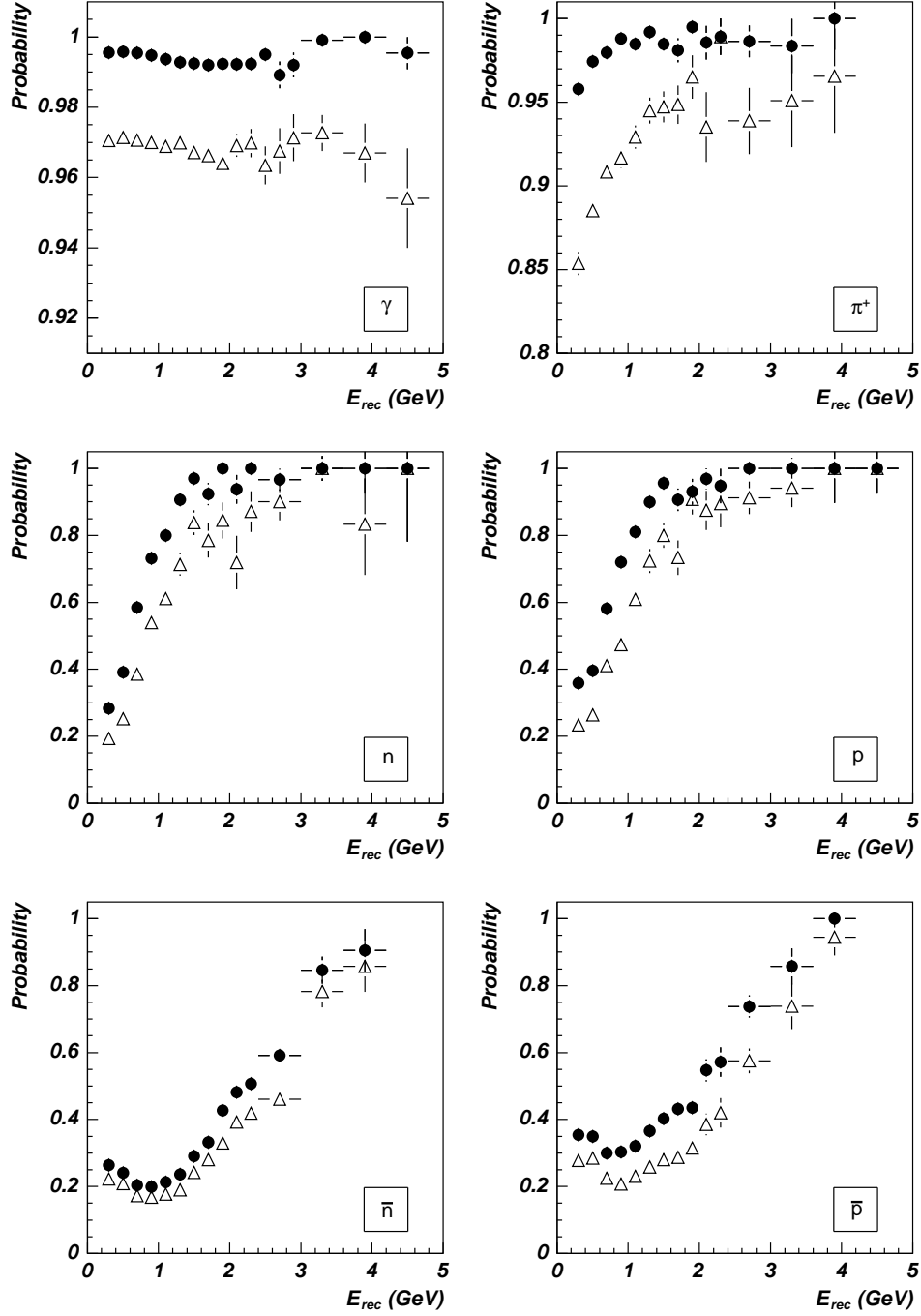
Figure 36: Probability of identifying a particle as a photon with high ($\triangle$) and low ($\bullet$) purity level by the TOF criterion as a function of the reconstructed energy for γ, n, $\bar{n}$, p, $\bar{p}$ and $\pi^{\pm}$ generated by HIJING simulations for Pb-Pb collisions at $5.5A$ TeV and $b < 5$ fm. Similar results obtained for $b < 2$ fm.
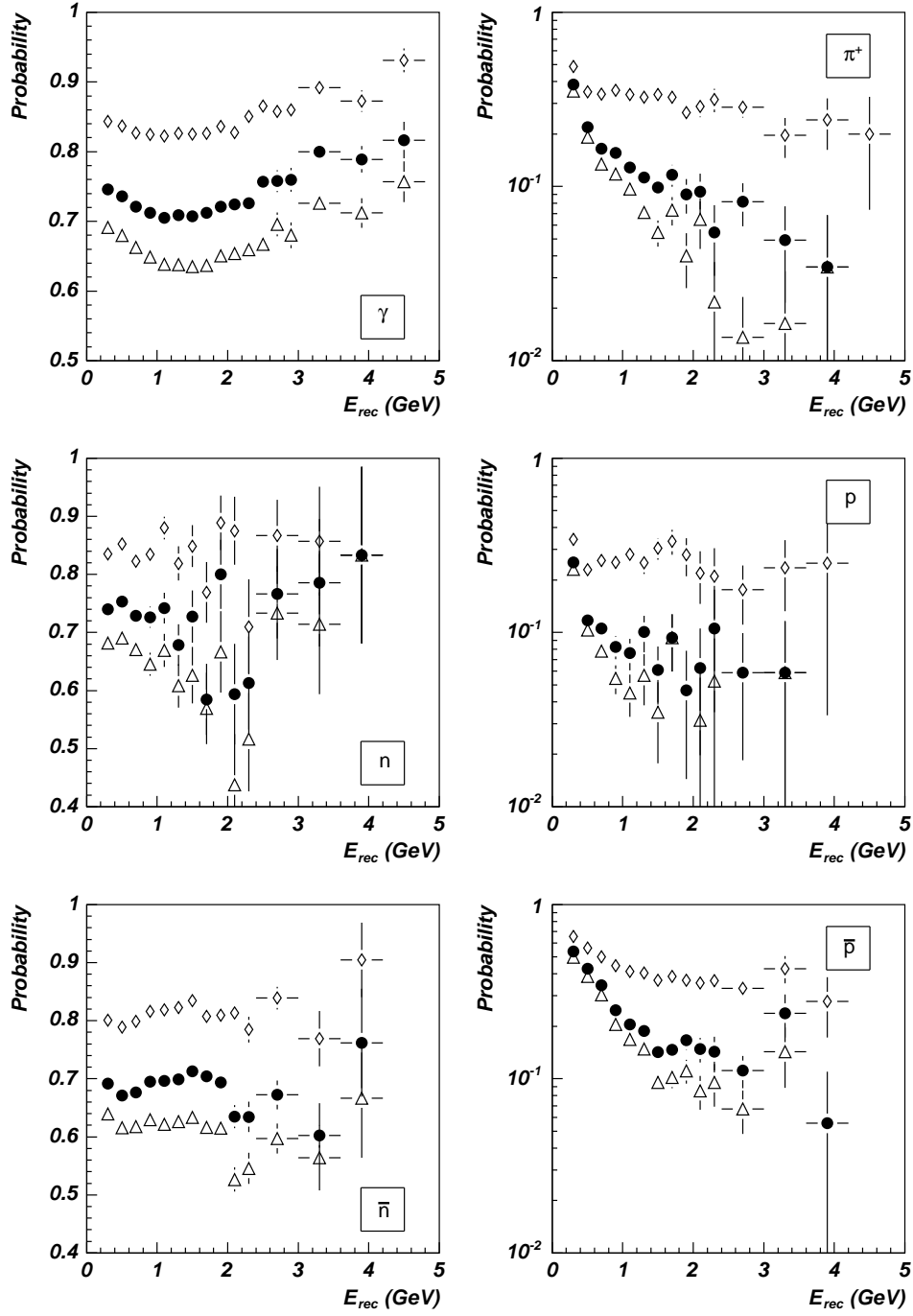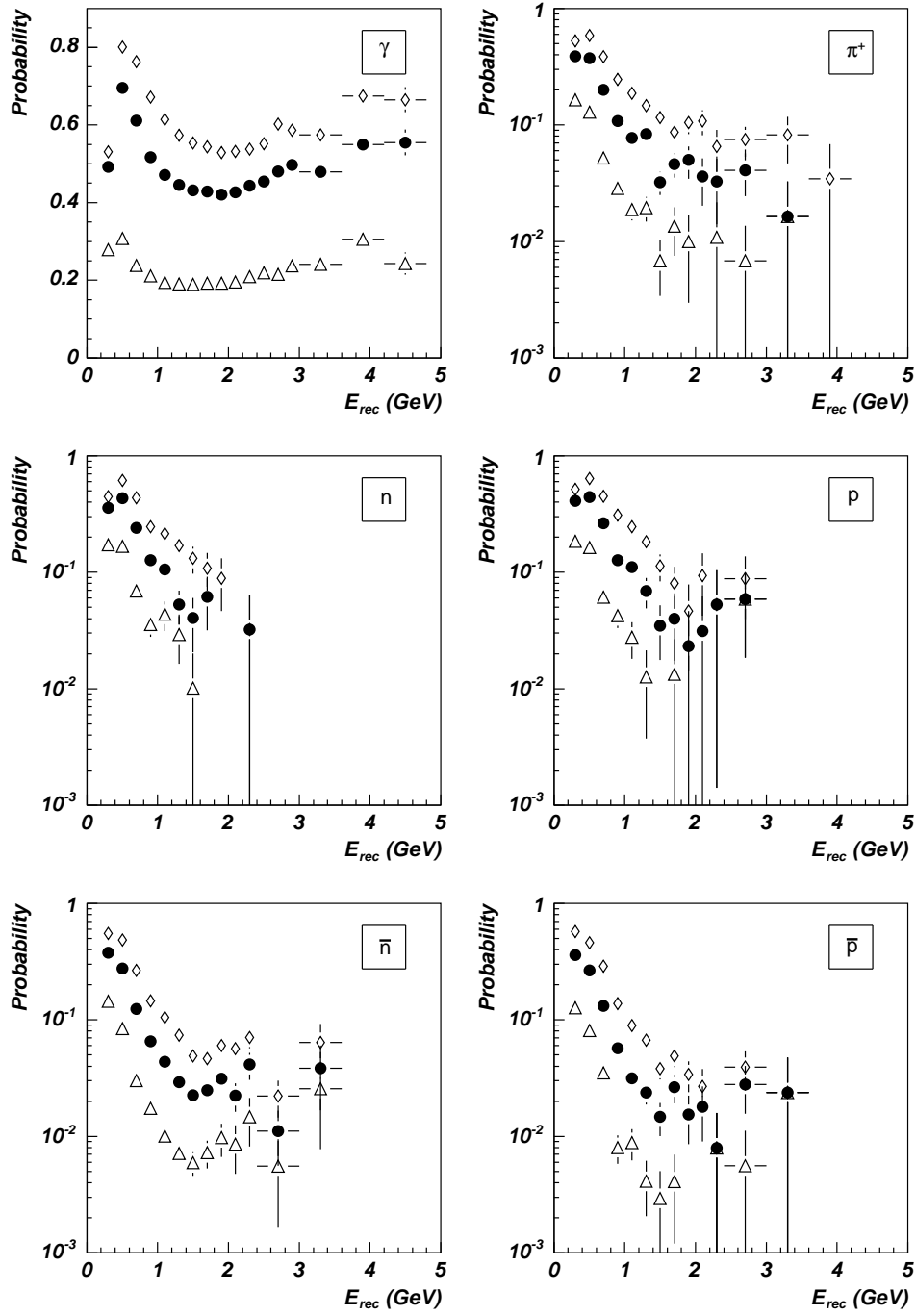
Figure 37: Probability of identifying a particle as a photon with high (△), medium (●) and low (◇) purity level by the CPV criterion as a function of the reconstructed energy for γ, n, $\bar{n}$, p, $\bar{p}$ and $\pi^{\pm}$ generated by HIJING simulations for Pb-Pb collisions at $5.5A$ TeV and $b < 5$ fm.
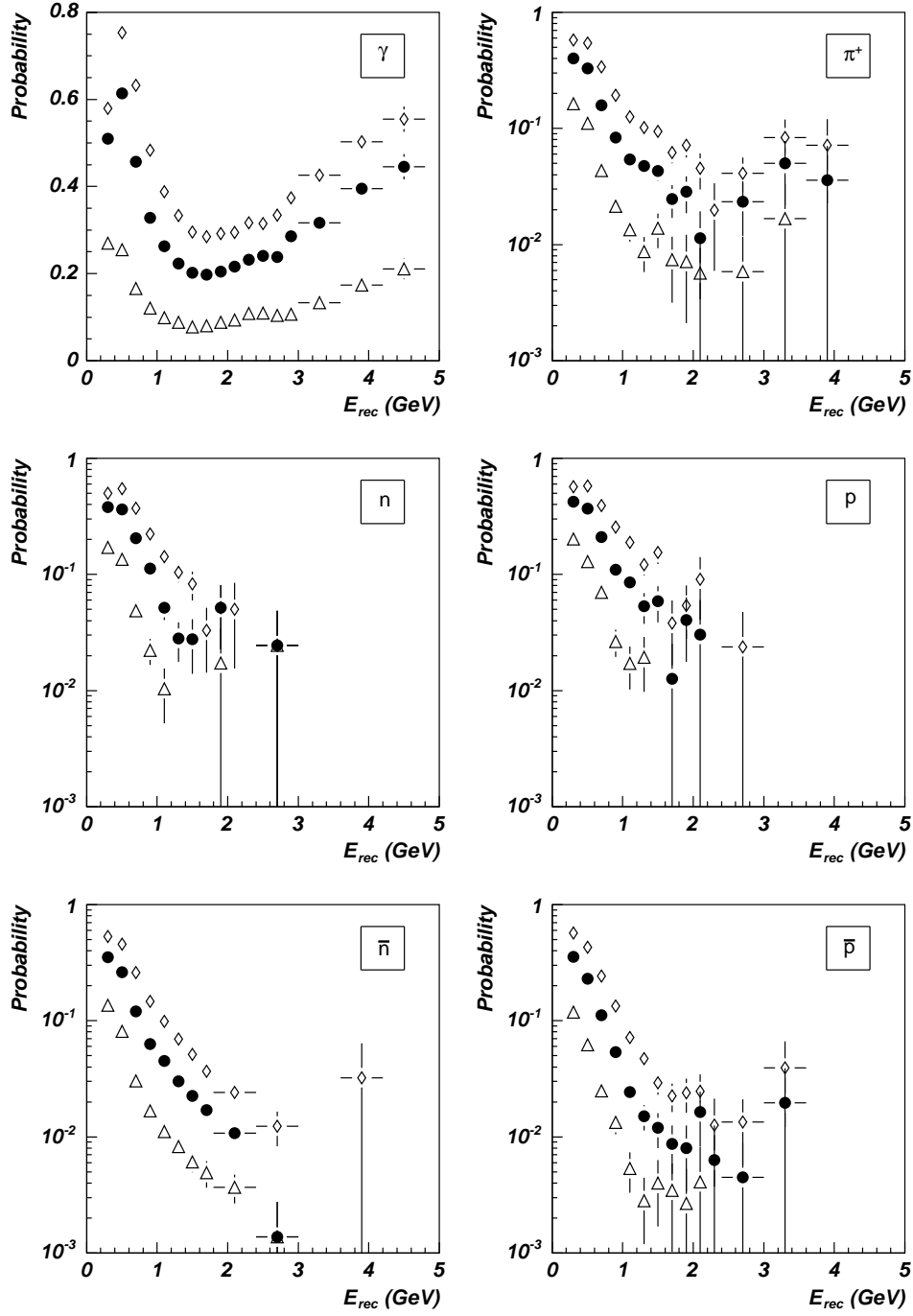
37
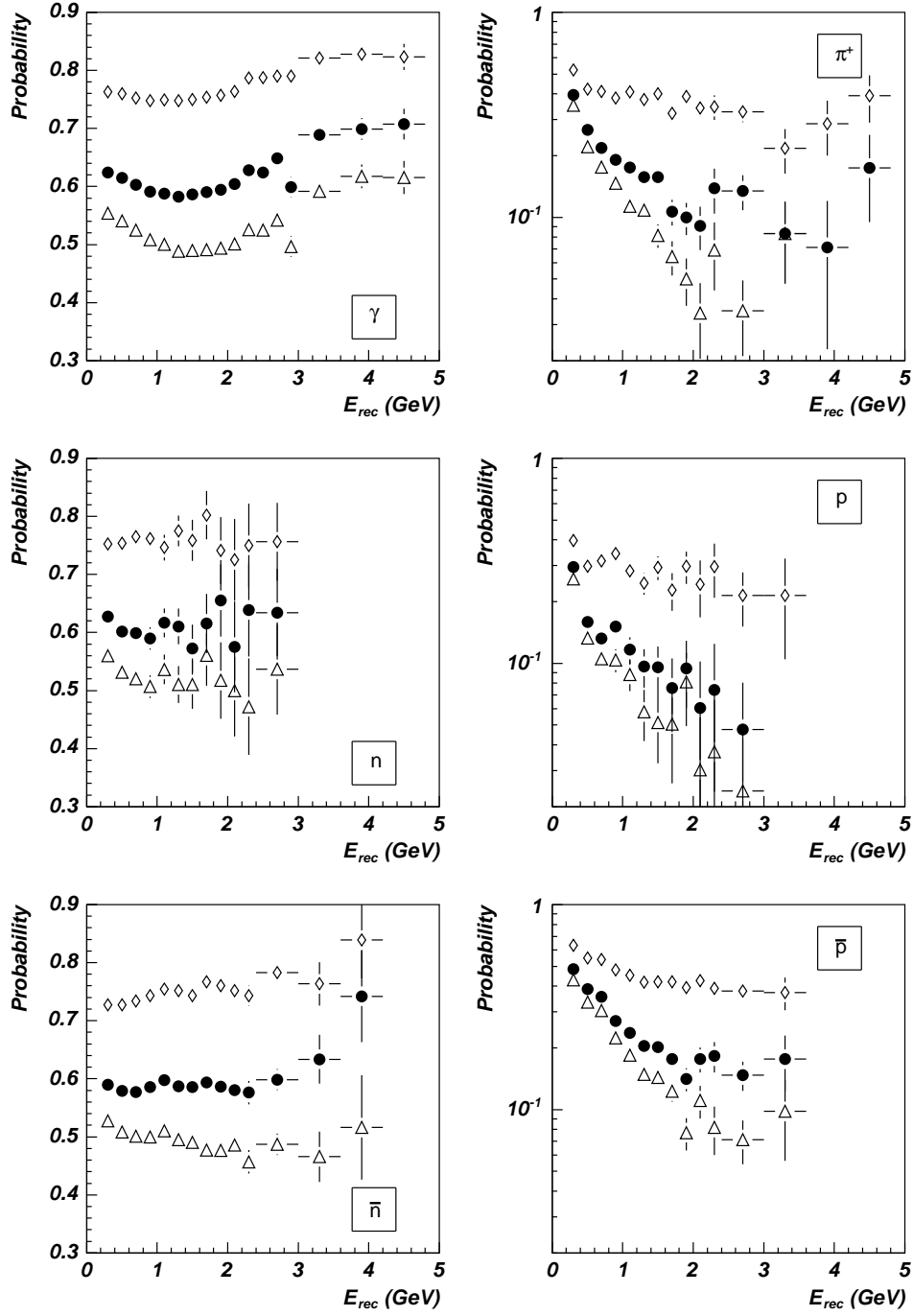
Figure 38: Probability of identifying a particle as a photon with high (△), medium (●) and low (◇) purity level by the CPV criterion as a function of the reconstructed energy for γ, n, $\bar{n}$, p, $\bar{p}$ and $\pi^{\pm}$ generated by HIJING simulations for Pb-Pb collisions at $5.5A$ TeV and $b < 2$ fm.

Figure 39: Probability of identifying a particle as a photon with high (△), medium (●) and low (◇) purity level by the PCA criterion as a function of the reconstructed energy for γ, n, $\bar{n}$, p, $\bar{p}$ and $\pi^{\pm}$ generated by HIJING simulations for Pb-Pb collisions at $5.5A$ TeV and $b < 5$ fm.

Figure 40: Probability of identifying a particle as a photon with high (△), medium (●) and low (◇) purity level by the PCA criterion as a function of the reconstructed energy for γ, n, $\bar{n}$, p, $\bar{p}$ and $\pi^{\pm}$ generated by HIJING simulations for Pb-Pb collisions at $5.5A$ TeV and $b < 2$ fm.

The comparison of the identification probabilities for each of the three identification criteria alone allows us to conclude that for energies $E < 1$ GeV the TOF criterion is the most efficient. The CPV criterion rejects charged hadrons for $E > 1$ GeV, while the PCA criterion rejects charged and neutral hadrons for $E > 1$ GeV.

In Figs. 41 and 42 the results for the three identification criteria combined are plotted. We observe that the probability of identifying photons has a maximum at low energies and then decreases reaching a minimum at about 1.5 GeV. If this probability is compared to the probability obtained by merging photons of energy uniformly distributed with HIJING events, shown in Fig. 43, we see that these probabilities are quite different. This difference is due on one side to the shape of the photon spectrum in HIJING events which is exponential and on the other side to the overlapping clusters produced in HIJING events. In these figures we observe a maximum of the identification probability at low energies and a decrease with energy which is more pronounced for HIJING events. This decrease is due to the overlapping of showers of different particles which produces reconstructed particles with higher energy than the original particle and photons identified as hadrons. Consequently, the probability denominator which is the number of clusters generated by photons, is enhanced at higher energies. In the case of single HIJING events, the probability decreases with the energy even faster due to the exponential shape of the HIJING photon spectrum. This effect is smaller and saturates for uniform energy photon distributions. On the other hand, if the photon spectrum is exponential, there is comparatively less high energy photons and an abrupt drop of the probability takes place.

The purity $\mathcal{P}$ of the identified photons is defined as the ratio of the number of reconstructed particles actually generated by photons and the total number of particles identified as photons. Similarly, the hadron contamination is defined as the ratio of the number of reconstructed particles identified as photons but generated by hadrons and the total number of particles identified as photons; obviously $\mathcal{C} = 1 - \mathcal{P}$. About $97 - 99\%$ of all the particles identified as photons are indeed photons. The contamination of photons is displayed in Fig. 44.

High-energy photons in a heavy-ion environment. The identification of high-energy photons in a HIC environment was studied with built-up test cases, simulated by mixing single hard photons of energy generated by a uniform distribution between 0.5 to 120 GeV with central Pb-Pb HIJING events ($b < 2$ fm and $b < 5$ fm). The identification probabilities of hard photons for heavy-ion collisions are plotted in Fig. 45. The hard photon identification probability decreases a 10 % compares with the single particle case due essentially to the failure of the CPV criterion.
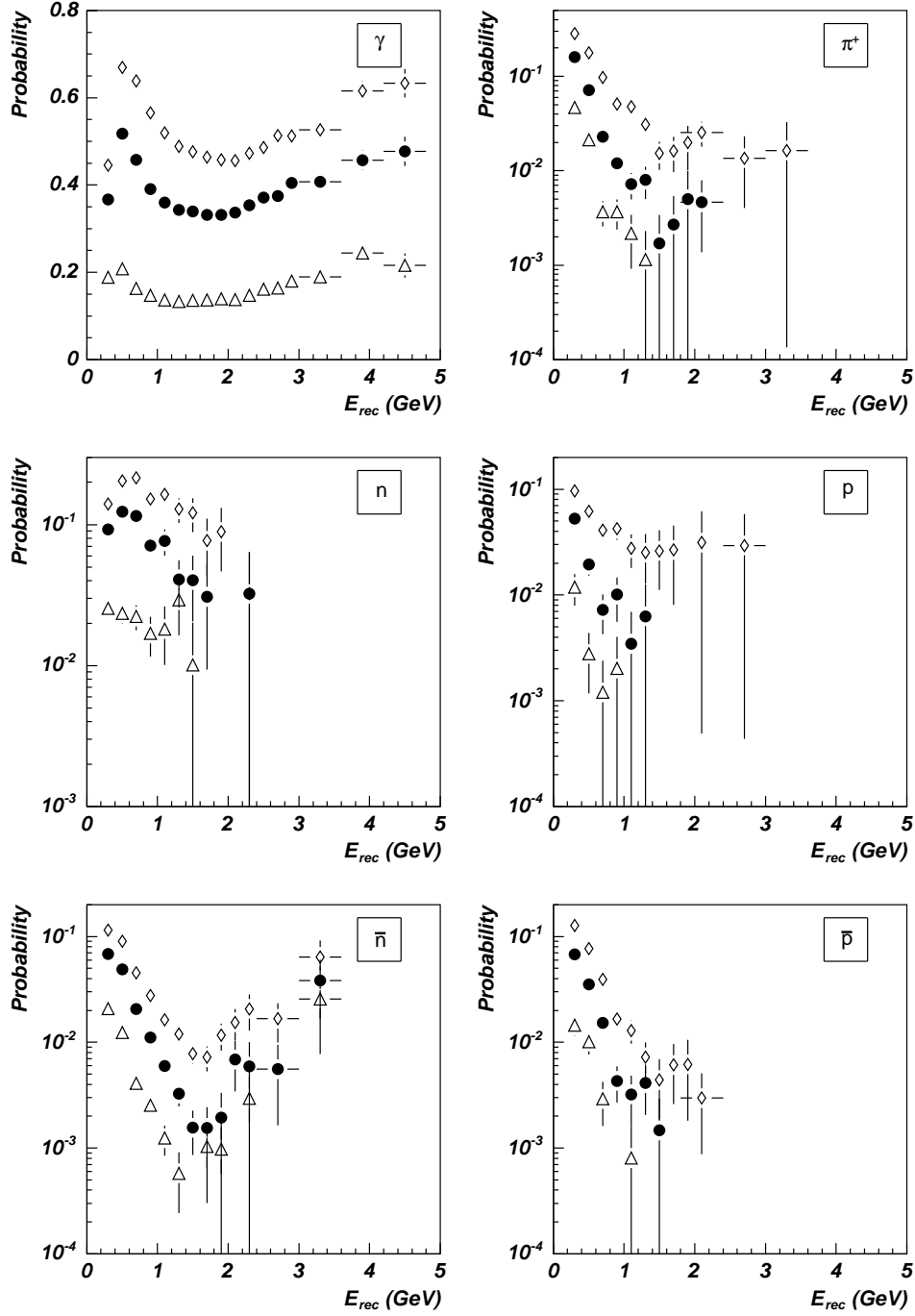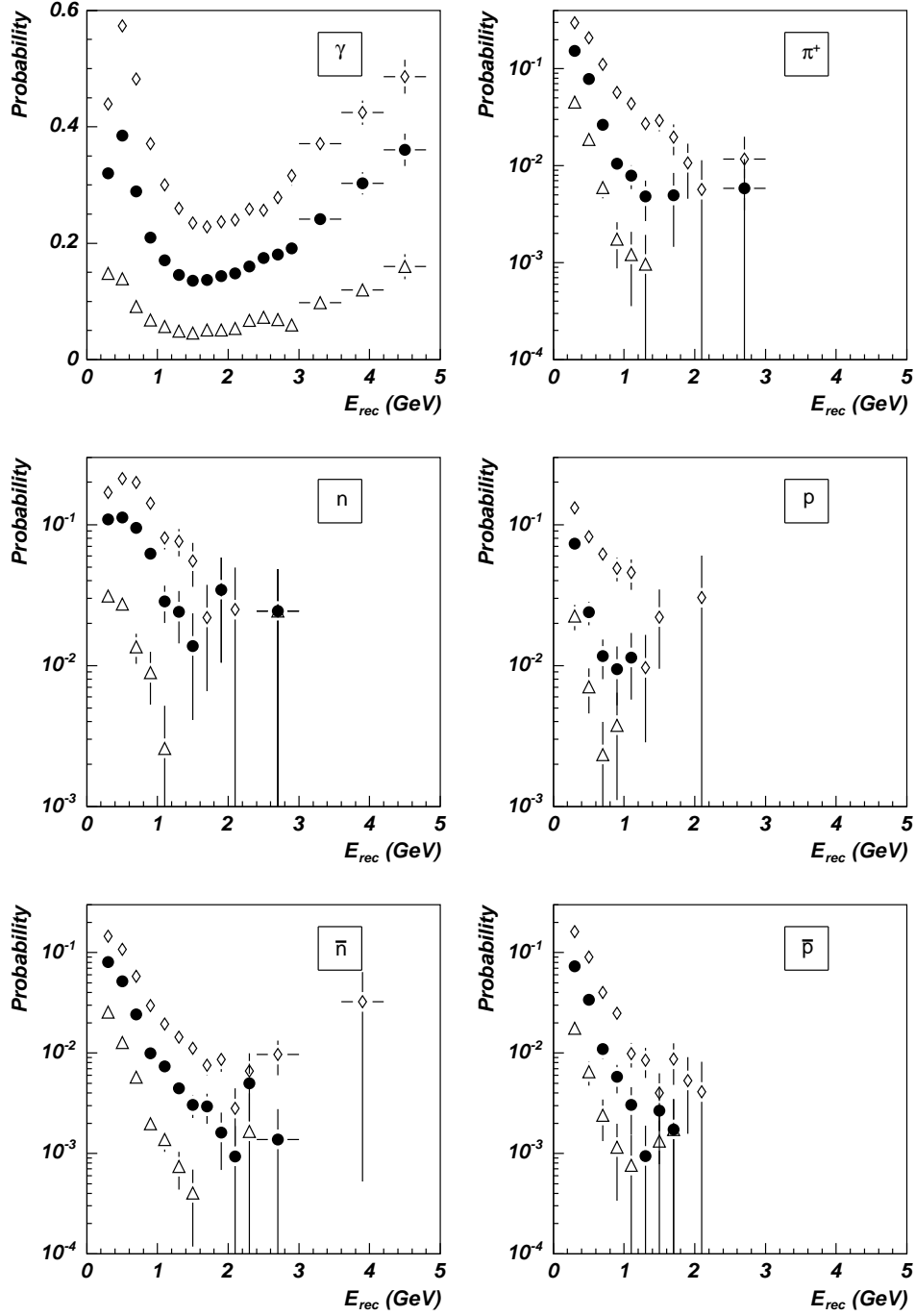
Figure 41: Probability of identifying a particle as a photon with high ($\triangle$), medium ($\bullet$) and low ($\diamond$) purity level by the TOF, CPV and PCA criteria as a function of the reconstructed energy for γ, n, $\bar{n}$, p, $\bar{p}$ and $\pi^{\pm}$ generated by HIJING simulations for Pb-Pb collisions at $5.5A$ TeV and $b < 5$ fm.

42

Figure 42: Probability of identifying a particle as a photon with high ($\triangle$), medium ($\bullet$) and low ($\diamond$) purity level by the TOF, CPV and PCA criteria as a function of the reconstructed energy for γ, n, $\bar{n}$, p, $\bar{p}$ and $\pi^{\pm}$ generated by HIJING simulations for Pb-Pb collisions at $5.5A$ TeV and $b < 2$ fm.

Figure 43: Probability of identifying photons generated with energy uniformly distributed from 0 to 5 GeV and merged with HIJING events as a function of the reconstructed energy with high ($\triangle$), medium ($\bullet$) and low ($\diamond$) purity level, for TOF, CPV and PCA criteria simultaneously required. Results for impact parameters $b < 5$ fm (left) and $b < 2$ fm (right) are shown.
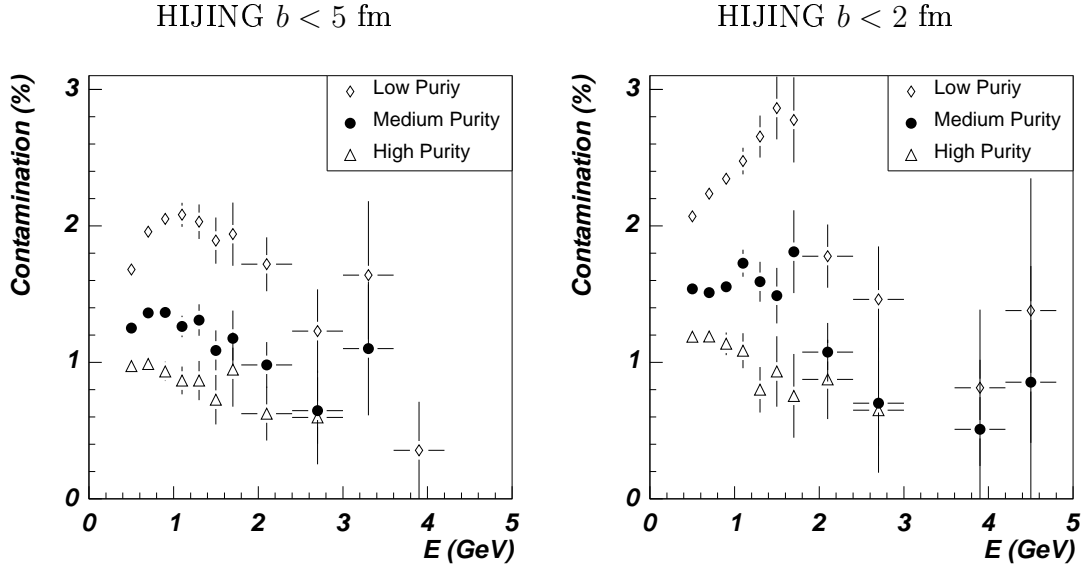
HIJING $b < 5$ fm   HIJING $b < 2$ fm

Figure 44: Hadron contamination of the spectrum of reconstructed particles identified as photons in HIJING events with $b < 5$ fm (left) and $b < 2$ fm (right) with high ($\triangle$), medium ($\bullet$) and low ($\diamond$) purity level.
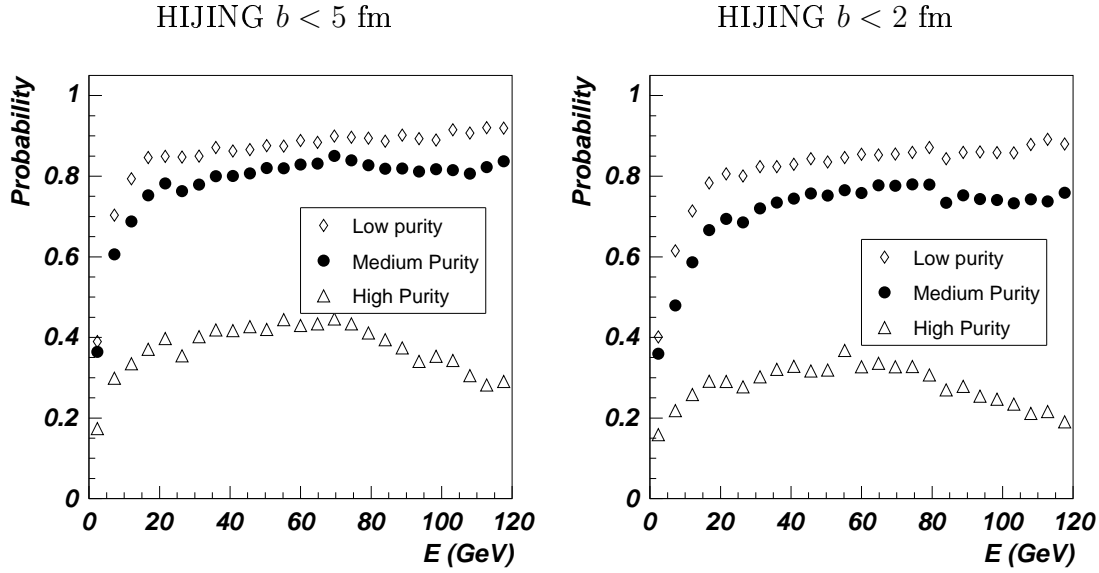
HIJING $b < 5$ fm HIJING $b < 2$ fm

Figure 45: Probability of identifying with high ($\triangle$), medium ($\bullet$) and low ($\diamond$) purity level of photons of energy uniformly distributed from 0.5 to 120 GeV and embedded in HIJING Pb-Pb collision events at $5.5A$ TeV with $b < 5$ fm (left) and $b < 2$ fm (right), for TOF, CPV and PCA criteria simultaneously required.

7 π^0 detection in PHOS

7.1 Invariant mass analysis of single π^0

Neutral mesons are identified by measuring in PHOS the two decaying photons and by applying the invariant-mass analysis (Fig. 46). The average mass resolution at the π^0 mass in PHOS is $3 - 6$ MeV/c^2 depending on the π^0 energy (Fig. 47). The probability to reconstruct π^0 by invariant-mass analysis, i.e. to distinguish the two decay photons and measure their invariant mass (Fig. 48), was evaluated from π^0 generated with a uniform energy distribution between 0 and 100 GeV and oriented toward PHOS so that both decay photons enter into the PHOS acceptance.

The reconstruction probability was studied for different gradual selections:

- without any selections (denoted as a bare efficiency);
- after applying a fiducial-volume cut, i.e. taking into account only those photons which are located at least 2 cells apart from the EMC edge;
- after applying a cut on two-photon invariant mass $|M_{\gamma\gamma} - M_{\pi^0}| < 2\sigma_{M_{\gamma\gamma}}$;
- after the asymmetry cut on the photon energies E_1 and E_2: $A = |E_1 - E_2|/(E_1 + E_2) < 0.8$;
- and, finally, after the photon identification with low, medium, and high purities.

We conclude that the π^0 spectrum can be measured in PHOS with a fairly good efficiency up to π^0 transverse momentum $p_T < 30$ GeV/c. Beyond this momentum value, the
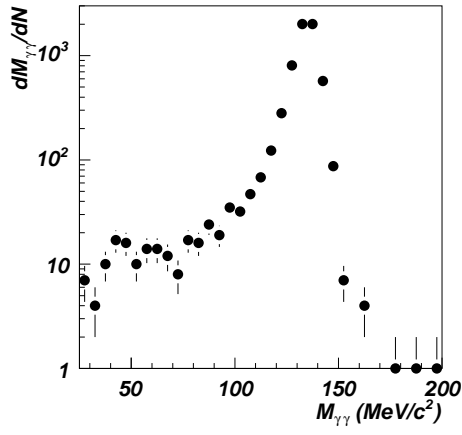
Figure 46: Invariant mass distribution calculated for photon pairs produced by the decay of π^0 with energies between 10 and 20 GeV.
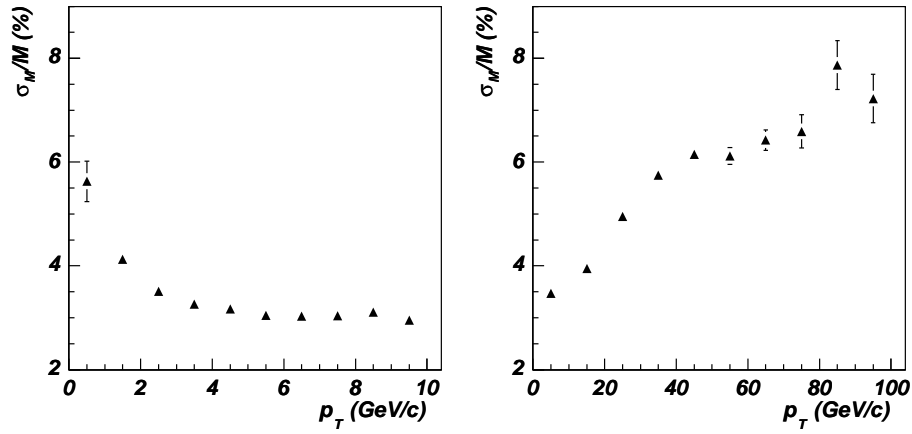

Figure 47: Invariant mass resolution calculated for π^0 of energy uniformly distributed between 0.5 and 100 GeV.
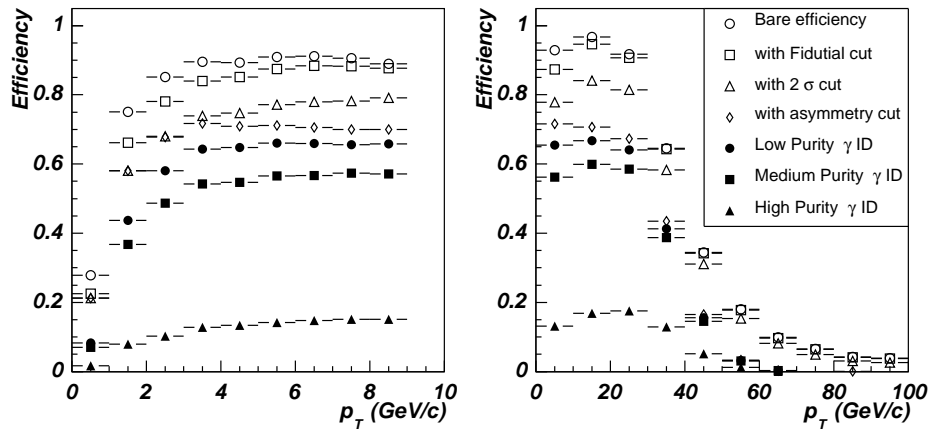

Figure 48: Probability of reconstructing π^0 by invariant-mass analysis with different conditions.

efficiency drops steeply and it vanishes above $p_T = 50$ GeV/c. This decrease is explained by the fact that the two decay photons merge into a single reconstructed point which cannot be unfolded anymore.

7.2 Invariant mass analysis of π^0 in the heavy-ion environment

The high π^0 multiplicity in a heavy-ion environment generates a combinatorial background in the invariant-mass spectrum constructed by combining by pairs all the detected photons. The background underlying the π^0 peak must be statistically subtracted. In central Pb-Pb HIJING collisions generated at impact parameter $b < 2$ fm, due to high combinatorial background, no peak at the π^0-mass is observed until pair transverse-momenta $p_T = 10$ GeV/c. This is because of the large contributions of hadrons which can be suppressed by applying a selection on the energy asymmetry parameter A. The decay-photons asymmetry distribution is uniform due to the isotropic π^0 decay. The distribution measured for all reconstructed particles in a HIJING event (Fig. 49)) exhibits a strong enhancement at large asymmetries and for large transverse momentum of a pair. This is explained by the combinations of very asymmetric particle pairs, where one particle is most probably a hadron. Eliminating pairs with these large asymmetries $A > 0.75$ reduces (Fig. 50) the combinatorial background significantly while the π^0 peak is suppressed by only 25%.
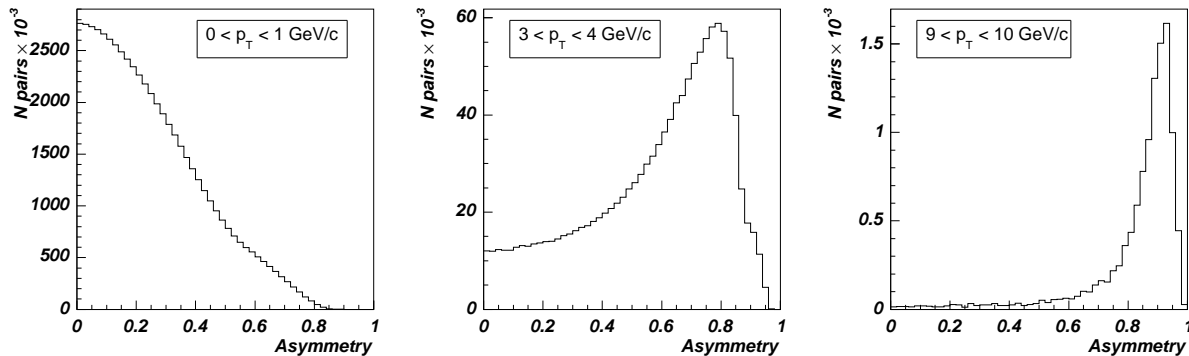

Figure 49: Energy asymmetry parameter A calculated for all reconstructed pairs generated in HIJING events and with transverse momenta $0 < p_T < 1$ GeV/c, $3 < p_T < 4$ GeV/c and $9 < p_T < 10$ GeV/c.

The procedure of the combinatorial background subtraction was demonstrated to be very efficient in the WA98 experiment [10] in Pb-Pb collisions at $158A$ GeV. According to this procedure, the combinatorial background is constructed in the event-mixing technique when all photon pairs for the invariant mass calculation are taken from different events to exclude any correlations. Applied to the ALICE heavy-ion environment, the procedure of the combinatorial background subtraction allows to extract the π^0 spectrum from above $p_T > 0.5$ GeV/c. As a demonstration, the invariant mass spectrum of all reconstructed
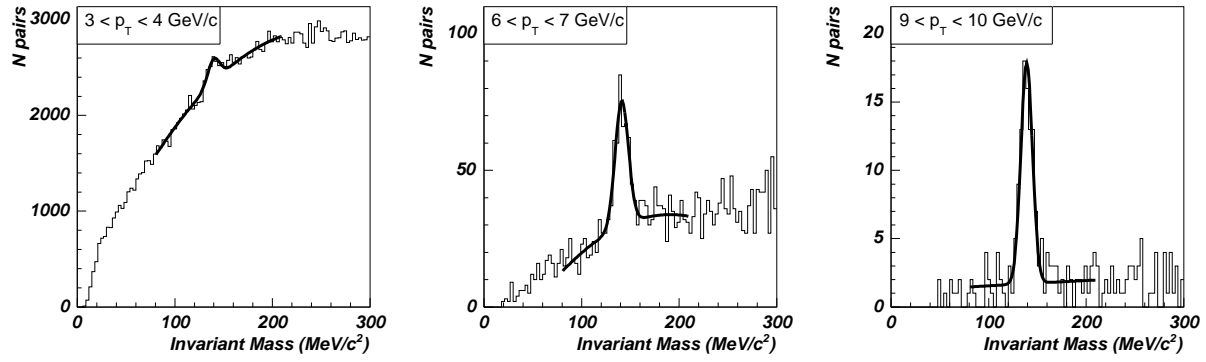
Figure 50: Invariant mass spectra in HIJING events of any reconstructed particle pairs with asymmetry $A < 0.75$ in the ranges $3 < p_T < 4\,\mathrm{GeV}/c$, $6 < p_T < 7\,\mathrm{GeV}/c$ and $9 < p_T < 10\,\mathrm{GeV}/c$.
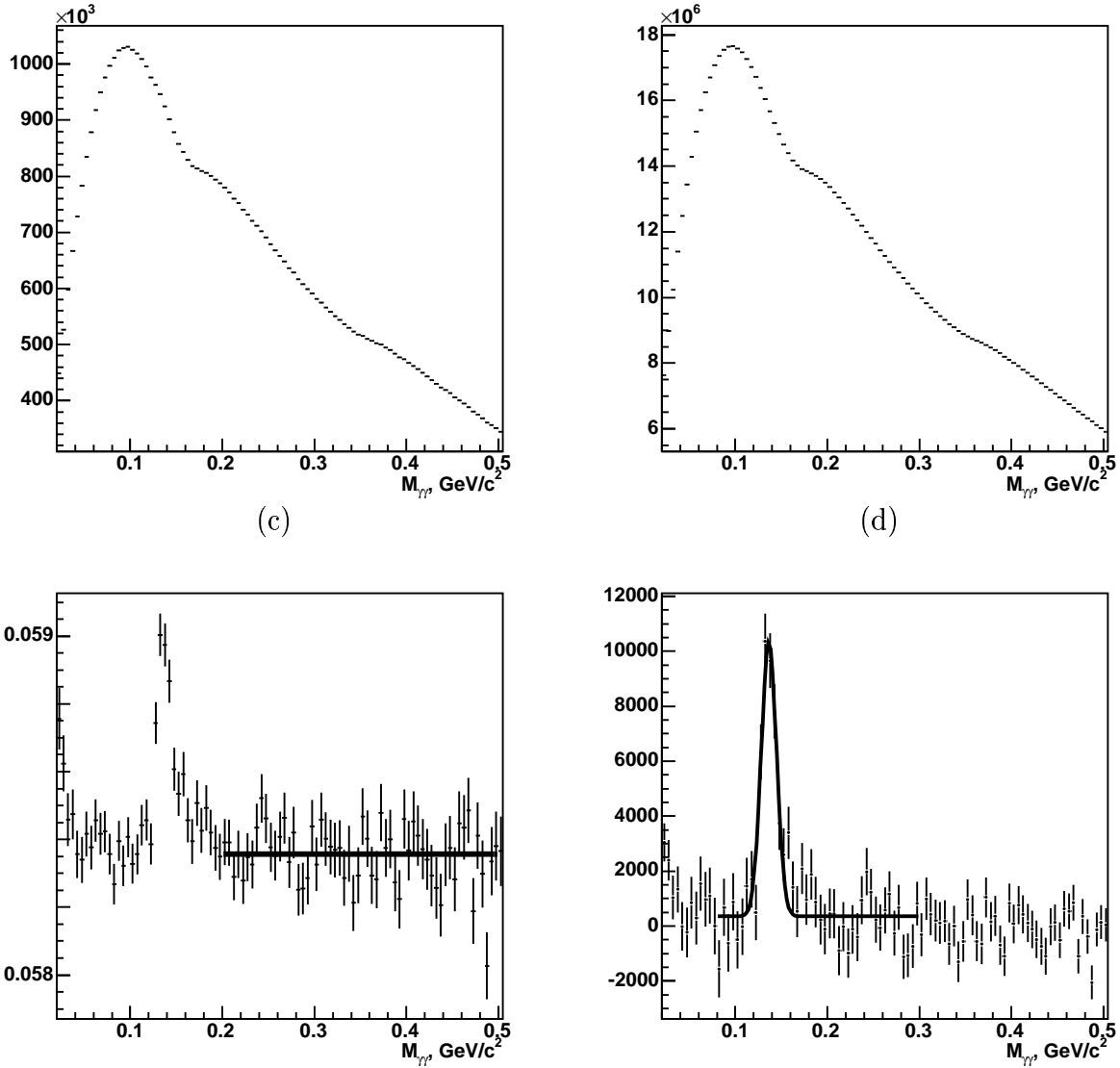

Figure 51: Two-photon invariant mass distributions in central Pb-Pb events (a), in mixed events (b), their ratio (c) and difference of the invariant- mass distribution and the combinatorial background (d). Transverse momentum of the $\gamma\gamma$ pairs in $1.0 < p_T < 1.5\,\mathrm{GeV}/c$. Statistics corresponds to 200,000 events.

.

48

particle pairs identified as low-purity photons, in 200,000 events of central Pb-Pb collisions at $b < 2$ fm, is shown in Fig. 51 (a) in the p_T-bin $1.0 < p_T < 1.5$ GeV/c. Due to the large combinatorial background the π^0-peak is not visible. Figure 51 (b) shows the invariant mass spectrum of reconstructed low-purity photons taken from 10 mixed events. The ratio of the invariant mass spectrum in Pb-Pb events to that spectrum in mixed events in Fig. 51 (c) reveals clearly visible peak at the π^0 mass. This ratio in the region of uncorrelated pairs between π^0 and η-meson peaks equal to $R = 0.0584$ is a scaling factor which normalizes mixed-event invariant mass spectrum to the mass spectrum in Pb-Pb events. The result of subtraction of the normalized mixed-event spectrum from the two-photon spectrum is shown in Fig. 51 (d). The statistical errors of the latter spectrum are propagated from the statistical errors of the spectra (a) and (b). The final two-photon mass spectra after the combinatorial background are fitted by the Gaussian, the dispersion of which is shown in Fig. 52 versus the π^0 transverse momentum.

The π^0 spectrum can be correctly reconstructed which is demonstrated by comparison of generated and reconstructed spectra (Fig. 53).
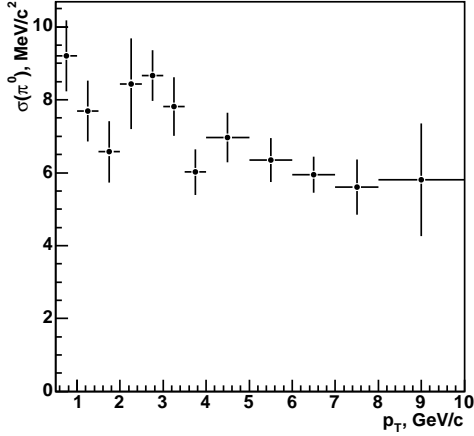
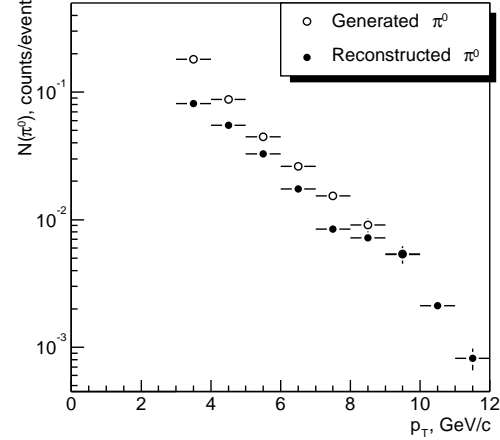Figure 52: Width of π^0 peak in central Pb-Pb collisions vs p_T.

Figure 53: p_T spectrum of generated and reconstructed π^0 per HIJING event.

	p_0	p_1	p_2	p_3
γ	0.17	54	9	1.3
π^0	1.5	$1.2 \cdot 10^{-3}$		

Table 6: Parameters obtained by fitting the M_{2x}^0 by Eq. (12) for high-energy photon identification and by a straight line for hard-π^0 identification.

8   Event by event photon/π^0 identification

At high momenta, π^0 are a priori identified as photons because the photons from π^0 decay merge into a single reconstructed point. Several approaches have been developed to discriminate these π^0 from photons. They are all based on the shower-shape analysis.

8.1   One-dimensional shower-shape analysis

Additional parameters need to be introduced to separate γ and π^0. The most helpful parameter to discriminate γ and π^0 is the second moment M_{2x} of the cluster, i.e. the largest eigenvalue of the covariance matrix ($M_{2x} = \lambda_1^2$ with $\lambda_1 \geq \lambda_2$, see Sec. 3.1) which is plotted in Fig. 54. At moderate E_{π^0} the M_{2x} distributions for photon and π^0 are well separated with only a slight overlap, while at higher p_T they merge into each other. To separate photons and π^0-mesons, the optimal cut M_{2x}^0 of the second moment distributions that maximizes the ratio of correctly identified to misidentified particles was determined. To get a reasonably high value of the identification probability, we restricted the search of this optimal cut to the interval between the mean values of the photon and π^0 moments and required a misidentification probability smaller than 3 %. The value of M_{2x}^0 is different for photons and π^0. This value as a function of the reconstructed energy is shown in Fig. 55. In this figure, M_{2x}^0 for photons was fitted by the equation

$$M_{2x}^0(\gamma) = p_0 \cdot \exp\left[\frac{(E - p_1)^2}{2 \cdot p_2^2}\right] + p_3, \tag{12}$$

and M_{2x}^0 for π^0 was fitted by a straight line. The p_i parameters of Eq. (12) for photons and of the linear fit for π^0 are given in Tab. 6.

The photon identification probability $P(\gamma, \gamma)$ is defined as the fraction of single-photon events with moment $M_{2x} < M_{2x}^0(\gamma)$, and the misidentification probability of π^0 as photons $P(\gamma, \pi^0)$ as the fraction of π^0 events with $M_{2x} < M_{2x}^0(\gamma)$. Similarly the π^0 identification probability $P(\pi^0, \pi^0)$ and the misidentification probability of photons as π^0 $P(\pi^0, \gamma)$ are defined as the fraction of π^0 and single photons with $M_{2x} > M_{2x}^0(\pi^0)$, respectively. These probabilities are shown in Fig. 56. The ratios $P(\gamma, \pi^0)/P(\gamma, \gamma)$ and $P(\pi^0, \gamma)/P(\pi^0, \pi^0)$ shown in Fig. 57 indicate that the misidentification probability is a few percent of the probability of correct identification at moderate p_T and not higher than
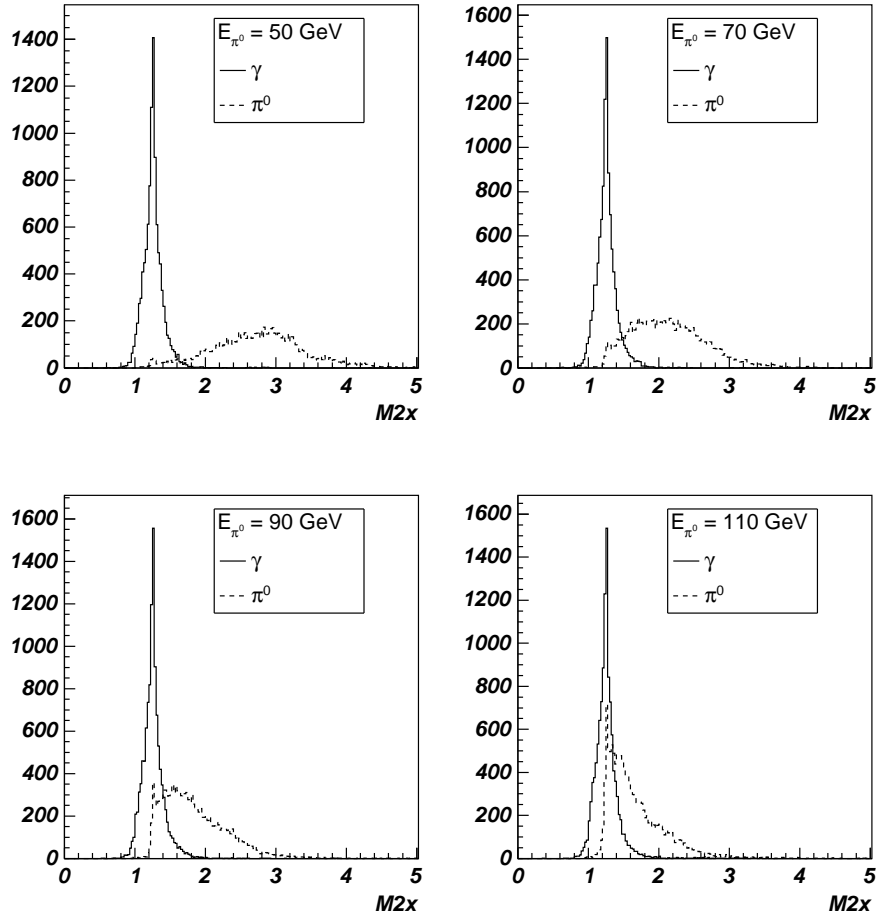
Figure 54: M_{2x} for photons (solid line) and π^0 (dashed line) of 50, 70, 90 and 110 GeV of energy.
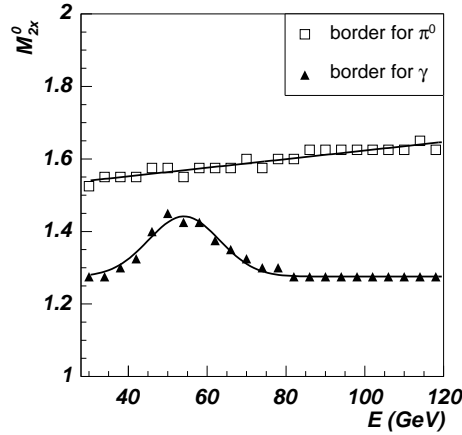

Figure 55: M_{2x}^0 threshold employed to separate photons from π^0 (▲) and π^0 from photons (□) as a function of the reconstructed energy. The photon threshold was fitted by Eq. (12) and the π^0 threshold was fitted by a straight line, with parameters given in Tab. 6.
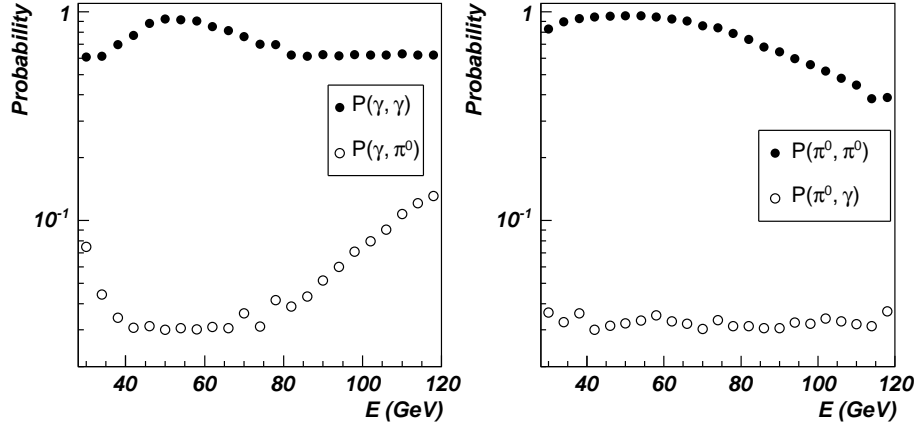
Figure 56: Probabilities of correct photon identification and π^0 misidentification as photon (left plot), and of correct π^0 identification and photon misidentification as π^0 (right plot).
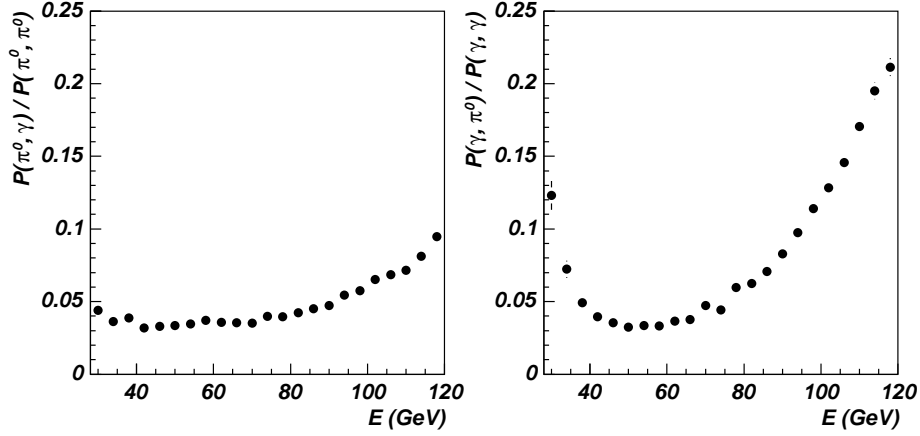

Figure 57: Ratios $P(\gamma, \pi^0)/P(\gamma, \gamma)$ (left plot) and $P(\pi^0, \gamma)/P(\pi^0, \pi^0)$ (right plot).

10-20 % at $p_T = 120$ GeV/c. We obtained similar probabilities for high-energy γ and π^0 merged in a HIC environment.

8.2   Identification of photons and π^0 by PCA

A different approach to distinguish photons and π^0-mesons is based on the PCA described in Sec. 6.1.3. Scatter plots of showers of π^0-mesons of 46, 66 and 90 GeV of energy and scatter plots of photon showers of 40, 60 and 80 GeV of energy versus the two most significant principal components are shown in Fig. 58. The ellipses were obtained as described in Sec. 6.1.3. The π^0 distributions shown in Fig. 58 were fitted by Eq. (11) with parameters depending on the reconstructed energy, plotted in Fig. 59. The ellipse parameters for low, medium and high purity levels were fitted to a parabola with coefficients given in Tab. 7. Photon and π^0 showers are well separated at low energies but at higher energies

52

	p_0	p_1	p_2
a	0.95	$7.6\cdot 10^{-3}$	$-7.1\cdot 10^{-5}$
b	3.4	-0.041	$1.7\cdot 10^{-4}$
c	0.36	0	0
x_0	-6.1	0.11	$-3.8\cdot 10^{-4}$
y_0	4.7	-0.09	$3.8\cdot 10^{-4}$

Table 7: Parameters obtained by fitting the different ellipse parameters of Fig. 59 by a parabola.

their scatter plots in the principal component space overlap.

The probabilities of correct identification and misidentification $P(\gamma, \gamma)$, $P(\pi^0, \pi^0)$, $P(\gamma, \pi^0)$ and $P(\pi^0, \gamma)$ are defined as in Sec. 8.1 and are shown in Figs. 60 and 61 for π^0 generated with energy uniformly distributed from 30 to 120 GeV.

Identification of photons and π^0 by PCA in a heavy-ion environment. We studied the π^0 identification probability in a heavy-ion environment by the PCA as described in Sec. 6.2 for hard photons. Events with a π^0-meson with transverse momentum uniformly distributed in the range $30 < p_T < 120$ GeV/c were merged with HIJING events for central Pb-Pb collisions. The probability of correct π^0 identification and of π^0 misidentification as photons are shown in Fig. 62, and the probability of correct photon identification and of photon misidentification as π^0 are shown in Fig. 63. These probabilities are only about a 10 % smaller than those of single photon and π^0 identification due essentially to the CPV matching failure (as observed in Sec. 6.2.2) for single hard photons, which means that the high detector occupancy existing in a heavy-ion environment does not modify significantly the capability of discriminating hard π^0 from photons by the PCA analysis.
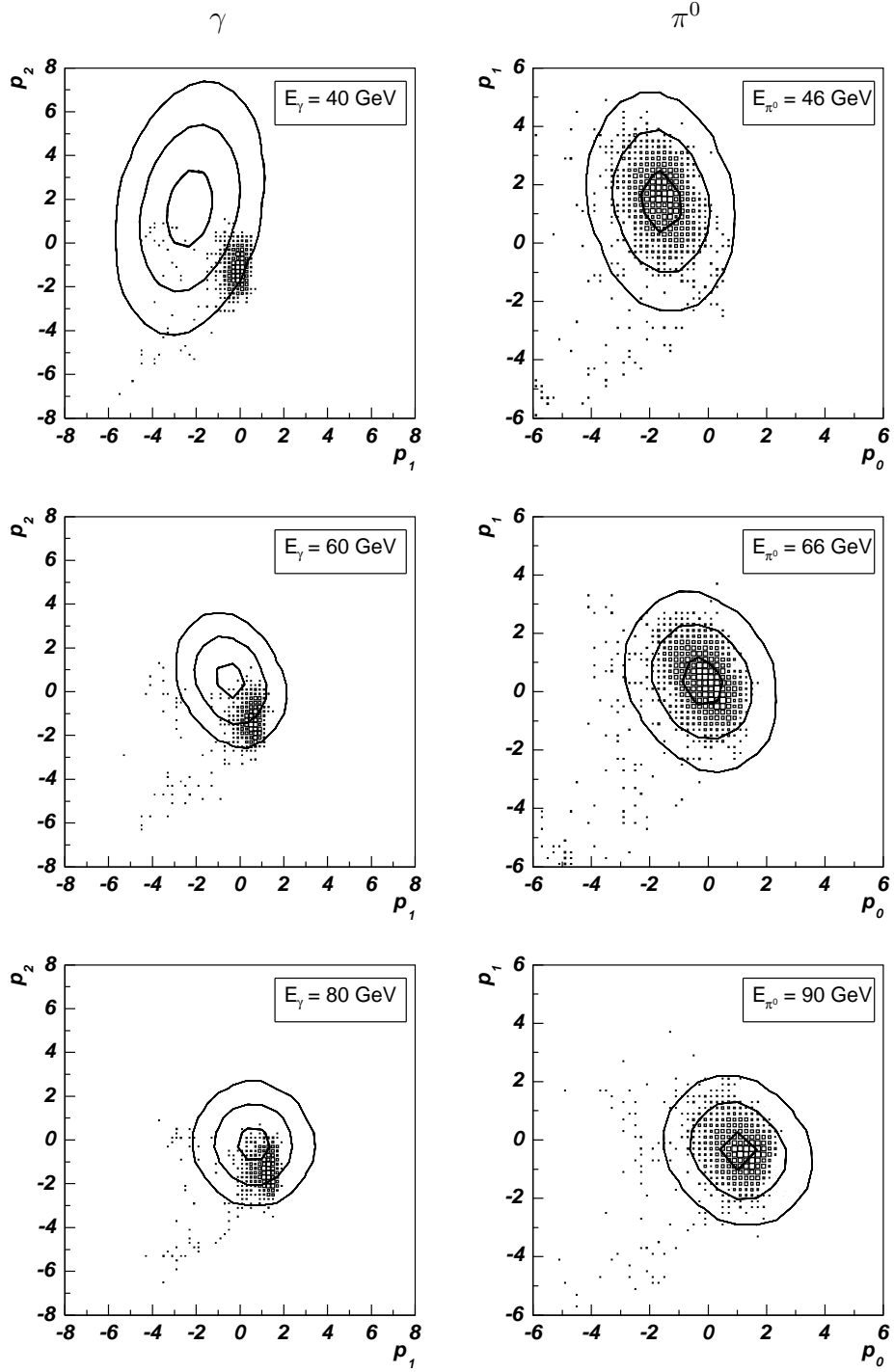
Figure 58: Scatter plots for γ showers of energies 40, 60 and 80 GeV (left) and π^0 showers of energies 46, 66 and 90 GeV (right) as a function of the the first two principal components obtained by the PCA. The three different ellipses show the high, medium and low purity contours for π^0 identification.
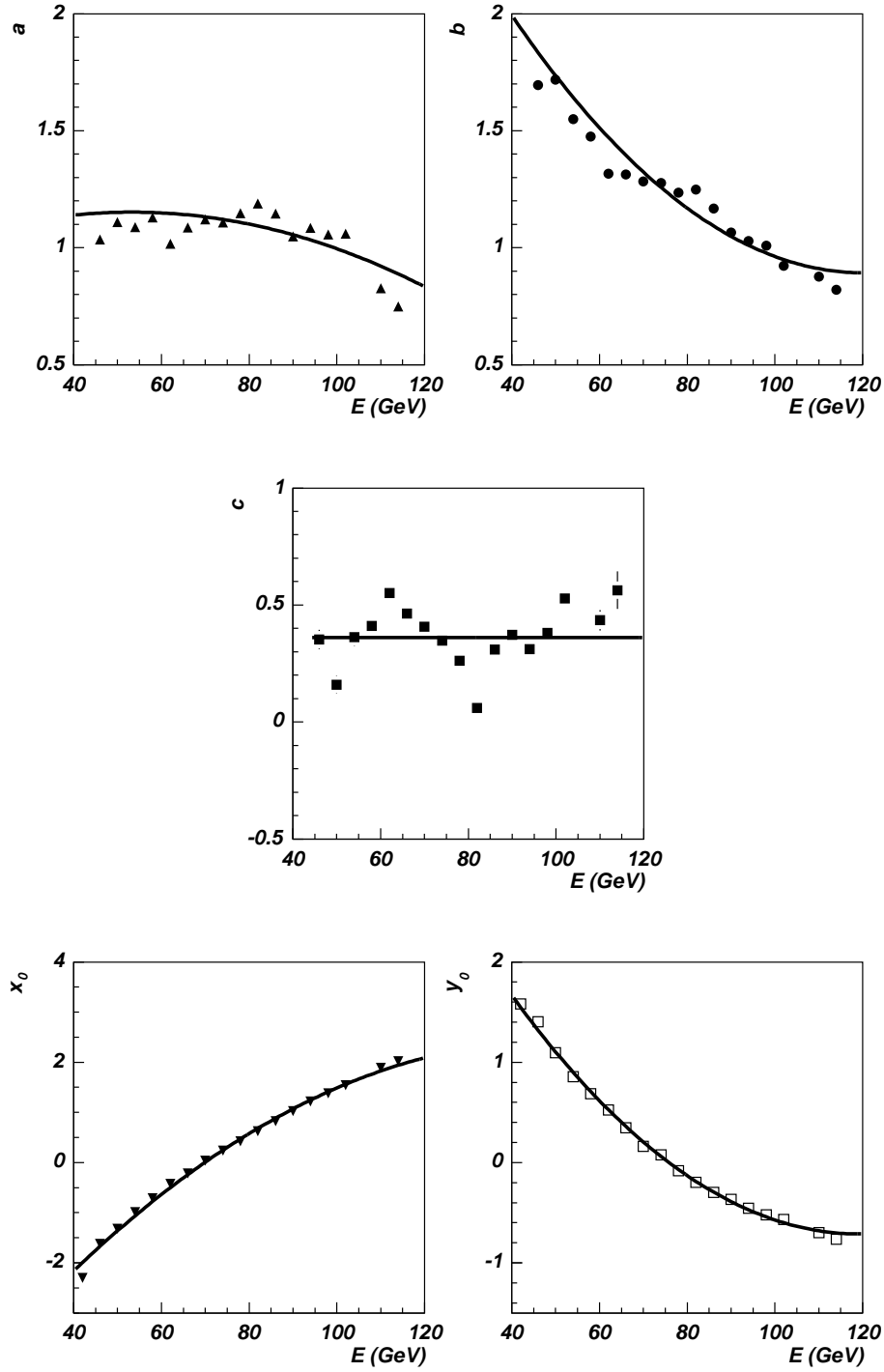
Figure 59: PCA ellipse parameters a, b, c, x_0 and y_0 vs reconstructed energy for π^0. Points were fitted to a parabola; the fitted parameters p_i are given in Tab. 7.
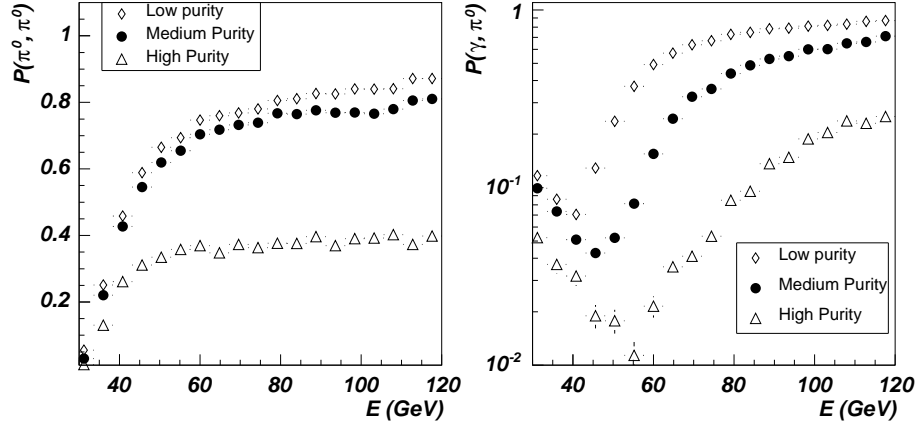
Figure 60: Probability of correct single π^0 identification (left) and misidentification as photons (right) by PCA for high ($\triangle$), medium ($\bullet$) and low ($\diamond$) identification purity levels.
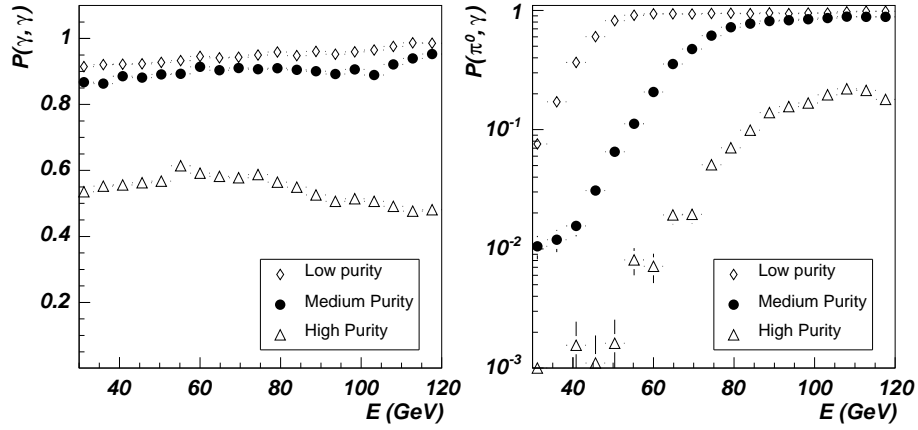

Figure 61: Probability of correct single photon identification (left) and misidentification as π^0 (right) by PCA for high ($\triangle$), medium ($\bullet$) and low ($\diamond$) identification purity levels.
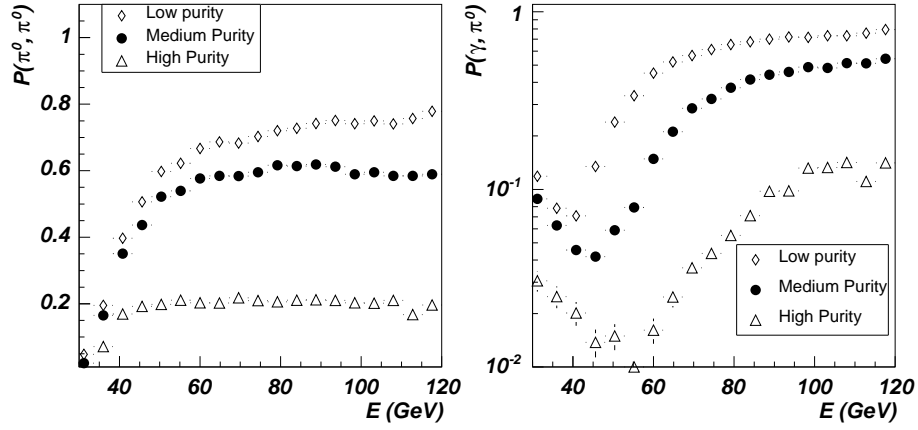
Figure 62: Probability of correct π^0 identification (left) and misidentification as photons (right) by PCA for π^0 embedded in a HIC environment (central HIJING events for Pb-Pb collisions at $5.5A$ TeV, $b < 2$ fm) with high ($\triangle$), medium ($\bullet$) and low ($\diamond$) purity levels.
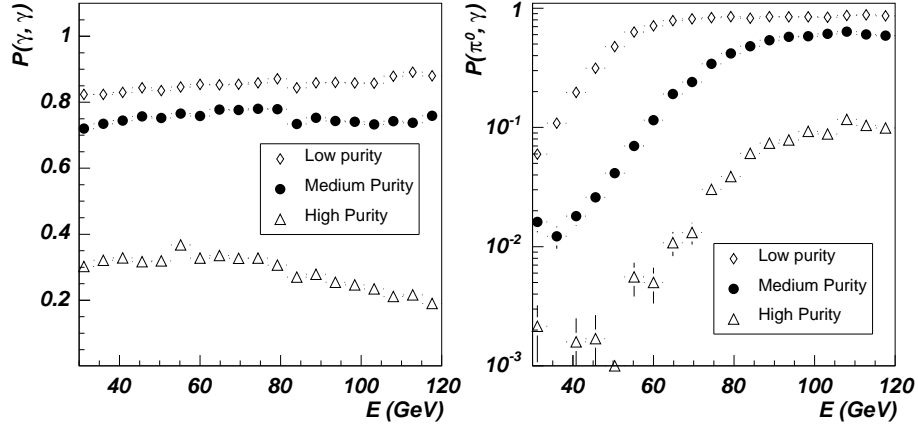

Figure 63: Probability of correct photon identification (left) and misidentification as π^0 (right) by PCA for simulated photons embedded in a HIC environment (central HIJING events for Pb-Pb collisions at $5.5A$ TeV, $b < 2$ fm) with high ($\triangle$), medium ($\bullet$) and low ($\diamond$) purity levels.
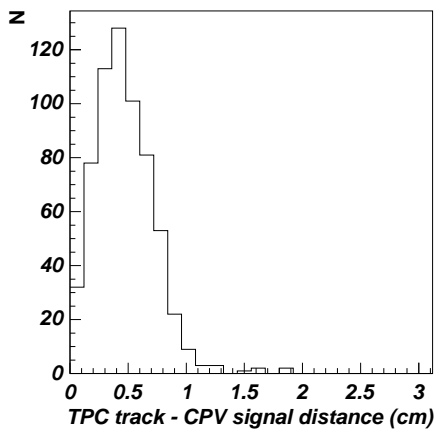
Figure 64: Distribution of the distance between the outer track in the TPC and the impact point in the CPV for electrons with energy uniformly distributed between 10 and 40 GeV.

9 Identification of high-energy photons converted into electron pairs

The presence of the TRD and TOF detectors in front of PHOS will perturb the photon yield detected in PHOS, as discussed in Sec. 5.4. Photons can interact with the material of these detectors and produce conversion electrons ($\gamma \to e^- e^+$). We discuss here how high-energy photons converted into electron pairs can be identified, and the impact of TRD and TOF to the converted $e^+ e^-$ pair identification in PHOS.

9.1 Converted photons reconstruction

The electrons created by a photon converted in the material between the TPC and PHOS can be identified because there is no matching track in the TPC pointing to the hit produced by those electrons in the CPV of PHOS. To minimize random matching in the heavy-ion environment, it is important to control accurately the matching criteria. For this purpose, electrons with energies between 10 and 40 GeV were simulated and the distance between the TPC track and CPV signal was studied. The distribution of the distance between the endpoint of the track in the TPC and the hit on the CPV is shown in Fig. 64. Although according to this figure, the maximum distance is about 2 cm, we have set the maximum to 4 cm in the matching algorithm to ensure that low-energy electrons which are more bent by the magnetic field are not rejected. More accurate simulations are needed to find the optimum value of the maximum matching distance.

In order to study the reconstruction of electrons produced by photon conversion, photons with energy uniformly distributed between 10 and 40 GeV for the setups with and without holes were generated. Particles identified as charged particles by the CPV but not detected by the TPC and identified as photons by the PCA were tagged as *conver-*
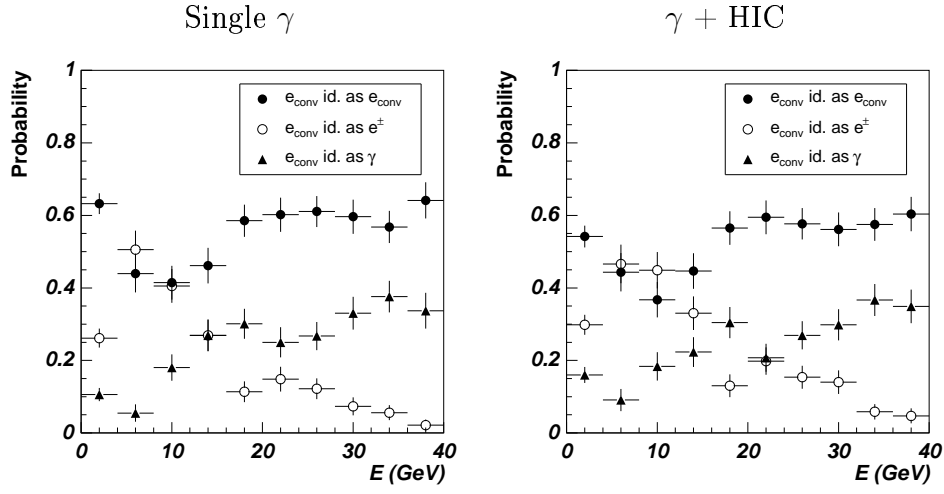
Figure 65: Probability of identifying electrons produced by conversion of photons in the material in front of PHOS as conversion electrons (●), electrons (○) and photons (▲). Results are shown for simulations of single photons with a uniform energy distribution from 10 to 40 GeV (left) and single photons merged with central HIJING events for Pb-Pb collisions at $5.5A$ TeV and $b < 2$ fm (right).

sion electrons. In this section, particles are identified as photons with low purity level; electrons are identified as low purity photons by the PCA and as charged particles by the CPV and the TPC. The probability of identifying conversion electrons as single photons is about 50-60 % in the energy range $E < 40$ GeV, as seen in Fig. 65.

In order to recover the original photons from the conversion electrons, the invariant mass of all possible pairs of identified conversion electrons was calculated. If the invariant mass was small, the pair came likely from a photon of energy close to the total energy of the pair. If only an isolated conversion electron was detected, we assumed that both electrons fly very close to each other and PHOS cannot separate them, so the energy of this isolated electron was taken as the energy of the parent photon. In Fig. 66, the invariant mass distribution of the conversion pairs is displayed, without and with a HIC environment. In the first case the invariant mass distribution peaks at 0-0.2 MeV/c^2 for reconstructed energies between 10 and 40 GeV. In the case of a HIC environment, the invariant mass distribution is broader and we identified as photons conversion pairs of invariant mass smaller than 20 MeV/c^2.

9.2   Photon identification in PHOS

According to the criteria mentioned above, photons in PHOS can be identified as photons, as converted e^+e^- pairs or single electrons. If the photon is identified as a e^+e^- pair, it will be considered as a photon, and its 4-momentum will be correctly measured. In the case that photons cannot be identified either as photon or e^+e^- pair, it cannot be added to the reconstructed photon spectrum. Obviously, if the photon converted into a e^+e^-

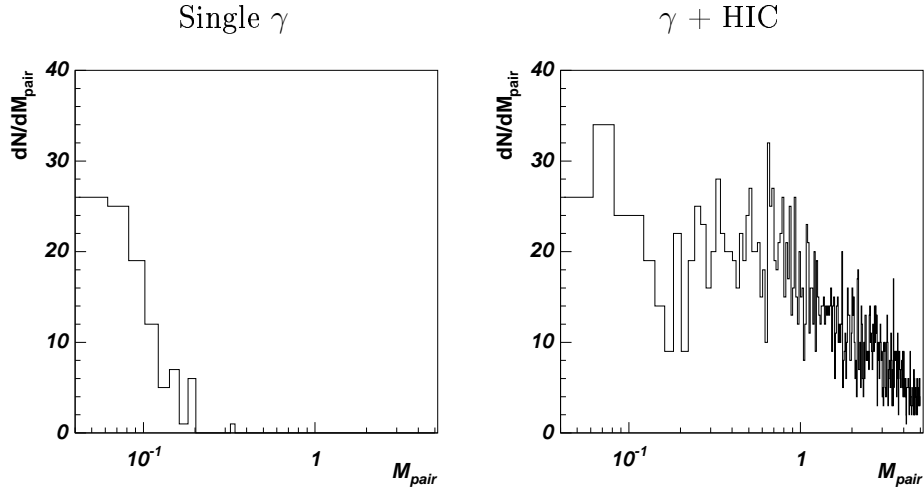Single γ $\gamma + $ HIC

Figure 66: Invariant mass of conversion electron pairs with energies between 10 and 40 GeV for simulated single photons (left) and simulated photons merged with a HIC environment (right).

pair is close to the PHOS surface, it will not be correctly identified.

Probabilities to identify photons as photons, converted e^+e^- pairs or single electrons are shown in Figs. 67 and 68 for the configurations without and with holes, respectively. Photons, conversion pairs and electrons were identified in PHOS as photons as stated above. If TRD and TOF are installed in front of PHOS, they will convert photons into e^+e^- pairs very close to the PHOS surface, and, thus, cannot be identified correctly. From these figures and Fig. 26 we conclude:

- In the configuration with holes, about 10 % of the photons suffer conversion somewhere between the interaction point and the CPV. Conversion electrons produced in the TPC are tagged mostly as electrons.

- In the configuration without holes about 30 % of the photons are converted into electrons, of which 20 % are converted in the TRD and TOF. Between 10 and 20 % of the photons can be recovered by conversion pair identification. If we add the identified conversion pairs to the identified photons, the identification probabilities for the configuration with and without holes are close.

The ratio of the number of identified photons to the sum of identified photons and conversion pairs is plotted in Fig. 69. We see in this figure that for single photons in the configuration without holes, the inclusion of conversion pair identification improves the photon identification by 20 %. For photons merged with HIC events, although apparently about 15 % of the photons are additionally recovered by including conversion pairs, what is actually identified as additional photons is mostly contaminating particles from the HIC background.
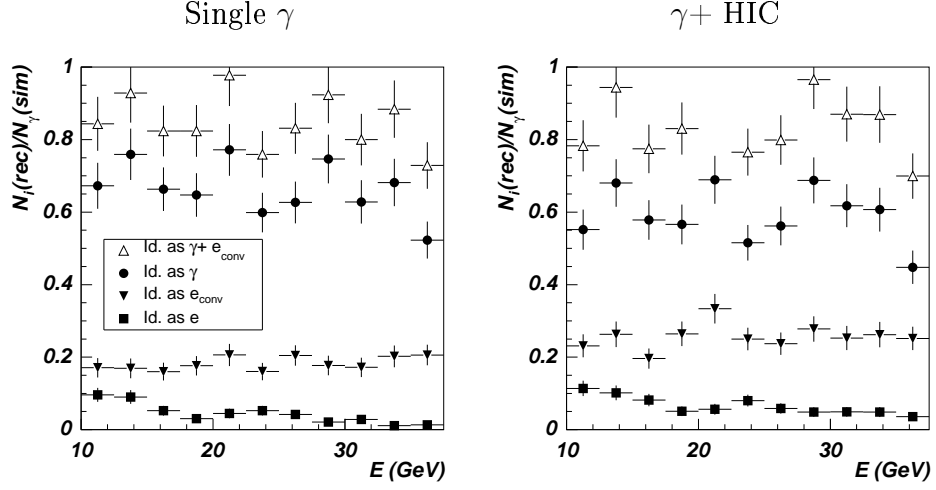
Single γ γ+ HIC

Figure 67: Probability of identifying photons as photons, conversion pairs or electrons for the setup without holes for single photons (left), and photons merged with HIJING events(right).
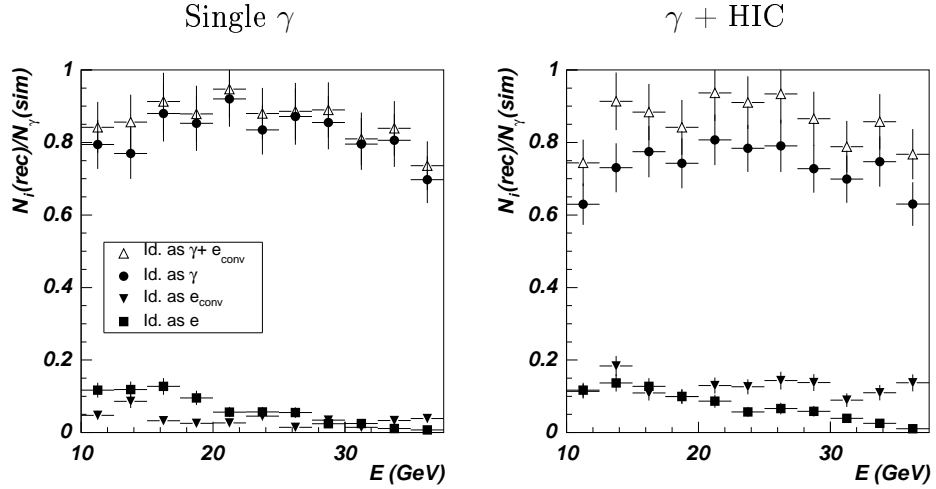
Single γ γ + HIC

Figure 68: Probability of identifying photons as photons, conversion pairs or electrons for the setup with holes for single photons (left) and photons merged with HIJING events (right).
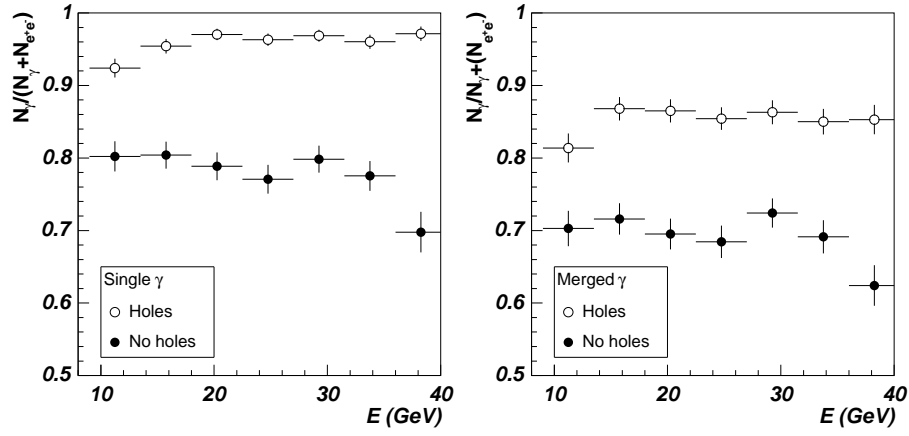
Figure 69: Ratio of particles identified as photons to particles identified as photons or conversion electron pairs with invariant mass smaller than 20 MeV for the setups with and without holes for single photons (left) and photons merged with HIJING events (right).

9.3   Neutral pion detection in PHOS

In this section, we study neutral pion identification along the lines of the previous section. Simulated π^0 mesons in the energy range 10-40 GeV for the setups with and without holes were generated. Pions were identified through the invariant mass of photon pairs; the invariant mass of photons and conversion pairs; by shower shape techniques, identifying overlapped photons as neutral pions. Figure 70 shows the identification probability of photon pairs from π^0 decay in the invariant mass window $0.1 < M_{pair} < 0.17$ MeV/c^2. The identification probability is about 70-80 % for the setup with holes and about 50-60 % for the setup without holes, in the energy range from 10 to 30 GeV. To identify π^0 in a HIC environment by the pair invariant mass, a more restrictive window is necessary. If we take $0.12 < M_{pair} < 0.15$ MeV/c^2 and an opening angle window as defined in Sec. 4.2 of Ref. [12] , the pair identification probability is reduced to 30-40 %, as shown in Fig. 71 for the setup without holes and in Fig. 72 for the setup with holes. We can summarize these results as follows:

- There is no significant improvement of the π^0 identification probability by the inclusion of converted pairs for the setup with holes.

- In the case of the configuration without holes, the inclusion of conversion pairs improves the single π^0 identification probability from about 20 % obtained without considering conversion pairs to about 40 %. In the case of a HIC environment, the neutral pion identification probability improves from about 15 % to about 30 %.

The ratio of the identification probabilities determined without and with conversion pair identification, shown in Fig. 73, indicates that the inclusion of converted pairs increases
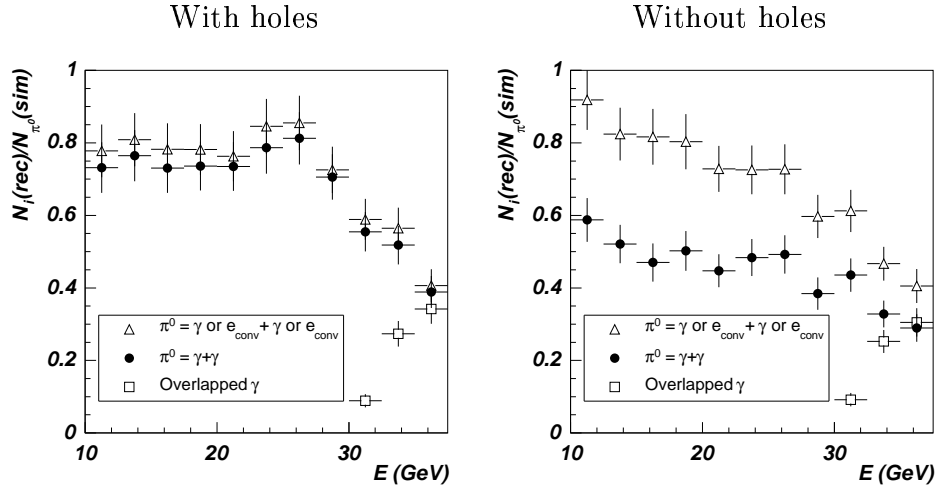
Figure 70: Probability of identifying single neutral pions by the invariant mass analysis with the invariant mass window $0.1 < M_{pair} < 0.17 \, \mathrm{MeV}/c^2$, and by the shower shape analysis (overlapped clusters), for the configurations with holes (left) and without holes (right). The probability for the invariant mass analysis is given for photon pairs ($\bullet$) and for photons and pairs of conversion electrons ($\circ$).

the single π^0 identification probability by about a 40 % for the setup without holes but by only a few percent for the setup with holes. In the case of a HIC environment, the apparent improvement is actually due to the background identified as conversion pairs.
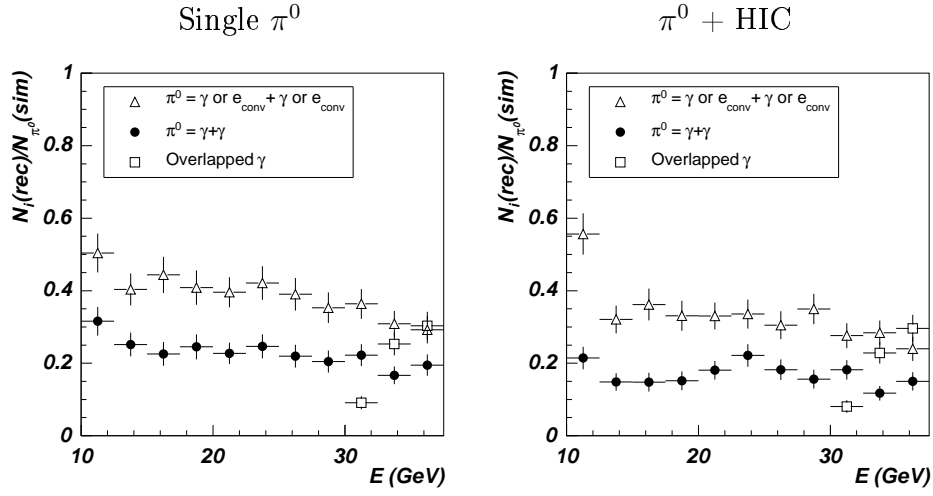
Figure 71: Probability of identifying neutral pions by the invariant mass analysis with $0.12 < M_{pair} < 0.15$ MeV/c^2 and opening angle defined in Sec. 4.2 of [12] and by the shower shape analysis (overlapped clusters), for the setup without holes. The probability for the invariant mass method is given for photon pairs ($\bullet$) and for photons and pairs of conversion electrons ($\circ$) for single π^0 (left) and π^0 merged with HIJING events (right).
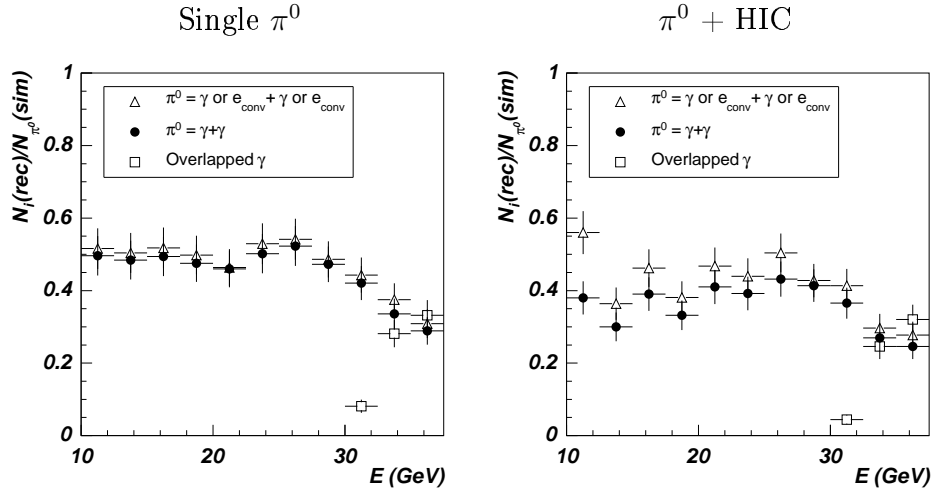

Figure 72: Probability of identifying neutral pions by the invariant mass analysis with $0.12 < M_{pair} < 0.15$ MeV/c^2 and opening angle defined in Sec. 4.2 of Ref. [12] and by shower shape analysis (overlapped clusters), for the setup with holes. The probability for the invariant mass method is given for photon pairs ($\bullet$) and for photons and pairs of conversion electrons ($\circ$) for single π^0 (left) and π^0 merged with HIJING events (right).
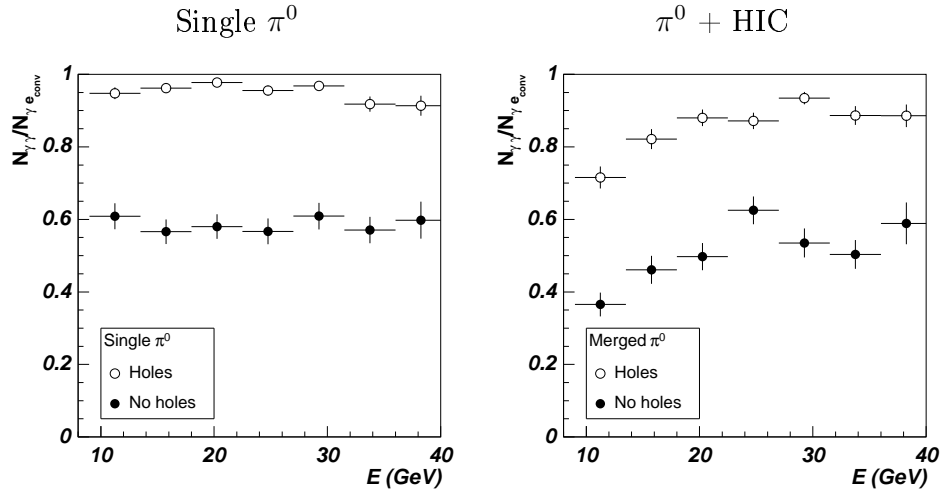
Single π^0

π^0 + HIC

Figure 73: Ratio of neutral pions identified by the invariant mass of photon pairs to neutral pions identified by both photon pairs and of photons and pairs of conversion electrons for the configurations with ($\circ$) and without ($\bullet$) holes for single π^0 (left) and π^0 merged with HIJING events (right).

Conclusions

The PHOS detector provides a good capability to detect and identify photons, electrons and π^0-mesons, and measure their 4-momenta with high precision.

PHOS simulation reproduces the beam-test experimental data which is confirmed by comparison of energy and position resolutions of PHOS sub-detectors.

Reconstruction algorithms of PHOS were adjusted to reduce systematics error in measuring the coordinates and energy of reconstructed points.

Implemented particle identification methods allow to identify photons and electrons and distinguish them from hadrons in a wide energy range from 0 to 100 GeV. Neutral pion spectrum can be measured in PHOS statistically by the invariant-mass analysis in the energy range from 0 to 40 GeV, and on event-by-event basis by particle identification at higher energies up to 100 GeV. Methods of photon-π^0 recognition at high energies were developed, and all of them demonstrate high identification efficiency of these particles up to 100 GeV.

References

[1] ALICE Collaboration, Technical Design Report PHOS, CERN/LHCC 99-4, ALICE TDR 2, Geneva, 1999.

[2] ALICE Collaboration, Physics Performance Report, chapter 3. J. Phys. G: Nucl. Part. Phys. **30** 1596-1691, (2004)

[3] A.M. Blick et al., Charged particle veto detector with open geometry for the PHOS spectrometer. ALICE Internal Note 2000–21 (2000).

[4] L. Aphecteche, H. Delagrange, D.G. d'Enterria, Y. Kharlov, G. Martinez, M.-J. Mora, D. Peressounko, and Y. Schutz, Predictions for high p_{t} γ and π^0 production at ALICE/LHC, ALICE Internal Note 2002–02 (2002).

[5] L. Aphecetche et al., PHENIX Collaboration, Nucl. Intr. Method. Phys. Res. A499, 521-536, (2003).

[6] Gyulassy, Miklos and Wang, Xin-Nian, HIJING 1.0: A Monte Carlo program for parton and particle production in high-energy hadronic and nuclear collisions, Comput. Phys. Commun. **83**, 307-331 (2004).

[7] H. Delagrange, D. d'Enterria, X. Li, G. Martínez, M.J. Mora, D. Peressounko and Y. Schutz, Improved Particle Identification in PHOS using a Pre-Shower Detector, ALICE Internal Note 2001–01 (2001).

[8] X. Camard, H. Delagrange, D. d'Enterria, Y. Kharlov, G. Martínez, M.-J. Mora, D. Peressounko and Y. Schutz, Screening PHOS or not: Impact on the Photon and Electron Physics, ALICE Internal Note 2001–27 (2001).

[9] R. Brun, M. Hansroul, J. Kubler. CERN preprint DD/EE/79-5 (1979).

[10] M.M.Aggarwal et al., WA98 collaboration. Nucl.Phys. A698 (2002) 135c–142c.

[11] G. Conesa and others, Bayesian approach for the identification of particles detected with PHOS, ALICE Internal Note 2005–16, (2005).

[12] G. Conesa et al, Prompt photon and photon-tagged jets identification with ALICE, ALICE Internal Note 2005–14, (2005).

[13] M.Yu. Bogolyubsky, Yu.V. Kharlov and S.A. Sadovsky, Direct Photon Identification with Artificial Neural Network in the PHOS, ALICE Internal Note 2003–37,(2003).